

Hodge-Laplacian of Brain Networks and Its Application to Modeling Cycles

D. Vijay Anand¹, Sixtus Dakurah¹, Botao Wang² and Moo K. Chung¹

¹University of Wisconsin, Madison, USA, ²Xi'an Jiaotong University, China

Abstract. Decoding the closed loops amidst a myriad of connections in a brain network is the key to understand the feedback and synchronization. The closed loops or cycles in a brain network embeds higher order signal transmission paths, which provide fundamental insights into the functioning of the brain. In this work, we propose an efficient algorithm for systematic identification and modeling of 1-cycles using persistent homology and the Hodge-Laplacian. We validate our methods on simulation and apply to human brain networks obtained through the resting state functional magnetic resonance images. New statistical inference procedures on 1-cycles are developed for discriminating male and female brain networks.

1 Introduction

Understanding the collective dynamics of brain networks has been a long standing question and continues to remain elusive. Many symptoms of the brain diseases such as schizophrenia, epilepsy, autism, and Alzheimer's disease (AD) have shown possible connections with abnormally high levels of synchrony in neural activity [1,2]. The mechanisms underlying the emergence of this synchronous behaviour, is often attributed to the higher order interactions that occur at multiple topological scales [3,4]. The higher order interactions are evidenced across multiple spatial scales in neuroscience such as collective firing of neurons [5], simultaneous activation of multiple brain regions during cognitive tasks [6]. The consideration of higher-order interactions can be highly informative for understanding neuronal synchronisation and co-activation of brain areas at different scales of the network [7]. Therefore uncovering and characterizing the dynamically changing structural and functional organization of brain networks across multiple resolutions is crucial.

Often graph theory based methods have been applied to analyzing the brain networks [8,9,10,11,12]. These models provide quantitative measures such as centrality [13,14], community detections [15] and hubs [16,17]. Although graph-based methods can be used to identify graph attributes at disparate scales ranging from local scales at the node level upto global scales at the community subgraph level, their power is limited to only pairwise dyadic relations [8]. The inherent *dyadic* assumption in graph theory limits the types of neural structure and function that the graphs can model [18,19]. Brain network models built on top of graphs cannot encode higher order interactions, i.e., three- and four-way interactions, beyond pairwise connectivity *without* additional analysis [20].

The hypergraphs facilitates to explore beyond pairwise interactions by using hyperedges. A hypergraph representation is the generalization of graph with an arbitrary group of nodes defining a hyperedge. The hyperedges allow for polyadic relations to be easily incorporated in the brain network [21]. Hypergraph based network representations are applied to functional brain imaging data to understand brain patterns in adaptability across task states [22], to quantify individual differences in brain functional dynamics [23], brain disease diagnosis [24] and detection of connectome biomarkers [25]. Since most hypergraph analysis rely on the extensions of graph-theoretic methods, it is often difficult to establish higher order analogues of several graph measures. Further, hypergraphs in dense connectivity setting often leads to a combinatorial explosion and causes a computational bottleneck even in modest network sizes [18].

More recently, topological data analysis (TDA) has emerged to be a powerful and one of the most sought-after data analysis techniques due to its simplistic construct in systematically extracting information from hierarchical layers of abstraction [26]. The algebraic topology in particular has mathematical ingredients that can effectively manipulate structures with higher order relations. One such tool is the *simplicial complex* which captures many body interactions in complex networks using basic building blocks called simplices [18]. The simplicial complex representation easily encode higher order interactions by the inclusion of 2-simplices (faces) and 3-simplices (volumes) to graphs. We can further adaptively increases the complexity of connectivity hierarchically from simple node-to-node interaction to more complex higher order connectivity patterns easily. The persistent homology (PH), one of TDA techniques deeply rooted in simplicial complexes, enables network representation at different spatial resolution and provides a coherent framework for obtaining higher order topological features [27,26]. The PH based approaches are becoming increasingly popular to understand the brain imaging data [28,29,30,31,32]. The main approach of PH applied to brain networks is to generate a series of nested networks over every possible parameter through a filtration. In literature, this persistent homological construct goes by the other names such as graph filtration or weight rank clique filtration [33]. The graph filtration is a concept specifically designed to uncover the hierarchical structure of the brain networks [34,35].

While the graphs, hypergraphs and simplicial complexes provide efficient representations of the interactions at different scales in the brain networks, it is important to associate statistical measures to these representations in order to achieve meaningful inferences from the brain network data. It is challenging to build a coherent statistical frameworks to transform these representations as quantitative measures to compare across brain networks by averaging or matching. Since most of our brain data is well defined on nodes (0-simplices) and edges (1-simplices), it is more rewarding to build higher order interactions nodes and edges somehow [7]. To this end, we focus our attention on 1-cycles which represents the most fundamental and natural form of a higher order interaction.

There have been several studies that consider brain network as the 1-skeleton of a simplicial complex, where the 0-dimensional hole is the connected component, and the 1-dimensional hole is a cycle [28,36,34]. Recently, the higher order simplicial complexes are used to represent and analyse the brain data [18,37,38,39]. The modular structure of network can easily be recognised by means of connected components, which is the first topological invariant that characterises the shape of the network[26]. The cycle on the other hand is a second topological invariant which are loops in the network. While the connected structures of the brain network has been extensively investigated, the studies on the cycles in modeling brain networks is very limited [3,34].

Generally, the presence of more cycles in a network signifies a dense connection with stronger connectivity. The cycles in the brain network not only determines the propagation of information but also controls the feedback [40]. Since the information transfer through cycles can occur in two different paths, it is sometimes interpreted as redundant connections. Further, it is also associated with the information diffusion and information bottleneck problems [41]. Although cycles in a network have been widely studied in graph theory, especially in path analysis, their importance in brain network analysis can be found in only few studies [42,42,43,44]. While cycles appear naturally in networks, it is not easy to extract or enumerate them. The cycles are often computed using the brute-force depth-first search algorithm [41]. Recently, a scalable algorithm for computing the number of cycles in the network was proposed [44]. The cycle or holes is usually identified by manipulating a matrix associated with the boundary operator in the persistent homology [45,46]. A better approach to determine cycles is by computing the eigenvectors corresponding to zero eigenvalues of higher order Laplacians [47], called p -Laplacian or Hodge Laplacian. The method represents the cycle as a linear combination of edges of which coefficients are proportional to their contributions to the cycle. This approach is essentially an extension of graph Laplacian (0-Laplacian) applied to nodes (0-simplices) to higher order simplexes [48]. Although these

algorithms are useful to extract cycles in small networks, it is computationally not feasible to construct and manipulate higher order simplices and extract cycles for large networks. Ideally, we need algorithms that can capture the essence of higher order interactions and yet retain the simplicity of graph-based approaches. This necessitates the need for new approaches that extends the power of graph theory coherently to higher dimensions. We believe the Hodge Laplacian (HL) based spectral approach is the solution to this holy grail.

In summary, to the best of our knowledge there is no efficient algorithm in literature to extract and enumerate cycles from brain networks. Recently, the Hodge theory based models have shown tremendous promise in extracting topological information of the cycles more efficiently. The spectral information of HL matrices embeds the simplicial homology (cycles) of the underlying network. To this end, we propose a new algorithm to efficiently extract 1-cycles using Hodge-Laplacian.

2 Method

2.1 Graphs as a simplicial complex

Simplicial complex Consider an undirected complete graph $G = (V, w)$ with vertex set V and edge weight matrix $w = (w_{ij})$ [10,31]. We assume there are p number of nodes. A binary graph $G_\epsilon = (V, w_\epsilon)$ is a graph consisting of the node set V and the binary edge weights $w_\epsilon = (w_{\epsilon,ij})$ given by

$$w_{\epsilon,ij} = \begin{cases} 1 & \text{if } w_{ij} > \epsilon, \\ 0 & \text{otherwise.} \end{cases} \quad (1)$$

Denote E_ϵ the edge set consisting of all the edges with nonzero weights. Then we may also represent the binary graph G_ϵ as $G_\epsilon = (V, E_\epsilon)$ if there is no confusion.

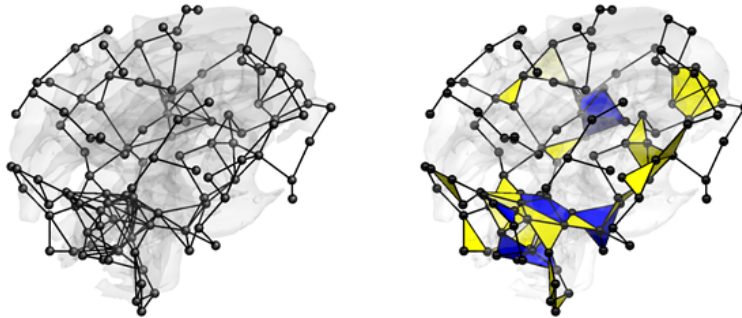


Fig. 1: (a) Illustration of brain network representation using graph and simplicial complex. The graph (left) has only nodes and edges. The simplicial complex (right) shows higher dimensional objects such as triangles (yellow) and tetrahedrons (blue) in addition to nodes and edges.

A p -simplex $\sigma_p = [v_0, v_1, \dots, v_p]$ is the convex hull of $p + 1$ algebraically independent points v_0, v_1, \dots, v_p :

$$\sigma_p = \left\{ \lambda_0 v_0 + \lambda_1 v_1 + \lambda_2 v_2 + \dots + \lambda_p v_p \mid \sum_{i=0}^p \lambda_i = 1, \lambda_i \in [0, 1] \right\}. \quad (2)$$

A simplicial complex is a collection of simplices such as nodes (0-simplices), edges (1-simplices), triangles (2-simplices), a tetrahedron (3-simplices) and higher dimensional

counterparts. More precisely, a simplicial complex K is a finite set of simplexes that satisfy two conditions: any face of a simplex from K is also in K ; the intersection of any two simplexes in K is either empty or a shared face [45]. A simplicial complex consisting of up to p -simplexes is called a p -skeleton. Thus, the graphs are 1-skeletons [49]. A simplicial complex can be viewed as the higher dimensional generalization of a graph [50,45,27]. Figure 1 illustrates the difference between graphs and simplicial complexes in representing a brain network.

Chain complex A p -chain is a sum of p -simplices in K denoted as

$$c = \sum_i \alpha_i \sigma_i,$$

where the σ_i are the p -simplices and the α_i are either 0 or 1 [45]. The collection of p -chains forms a group and the sequence of these groups is called a chain complex. To relate chain groups, we denote a boundary operator $\partial_p : C_p \rightarrow C_{p-1}$, where C_p denotes the p -th chain group. For an oriented p -simplex σ_p with the ordered vertex set, the boundary operator is defined as

$$\partial_p \sigma_p = \sum_{i=0}^p (-1)^i [v_0, v_1, \dots, \widehat{v}_i, \dots, v_p],$$

where $[v_0, v_1, \dots, \widehat{v}_i, \dots, v_p]$ is a $(p-1)$ -simplex generated from $\sigma_p = [v_0, v_1, \dots, v_p]$ excluding \widehat{v}_i . The boundary operator maps a simplex to its boundaries. Thus, $\partial_2 \sigma_2$ maps a triangle to its three edges. We can algebraically show that [45]

$$\partial_{p-1} \partial_p \sigma_p = 0.$$

Cycle A p -cycle is a p -chain whose boundary is zero. In a graph (1-skeleton), 1-cycles are loops and 0-cycles are the number of nodes. To compute p -cycles, we use the kernel and image for the boundary operator and establish their relation to the p -cycle [45,51]. Let Z_p be the collection of all the p -cycles given by

$$Z_p = \ker \partial_p = \{\sigma_p \in C_p \mid \partial_p \sigma_p = 0\}.$$

Let B_p be the boundaries obtained as

$$B_p = \text{img} \partial_{p+1} = \{\sigma_p \in C_p \mid \sigma_p = \partial_{p+1} \sigma_{p+1}, \sigma_{p+1} \in C_{p+1}\}.$$

Since any boundary $\partial_{p+1} \sigma_{p+1} \in B_p$ satisfies $\partial_p \partial_{p+1} \sigma_{p+1} = 0$, it is a p -cycle and $B_p \subset Z_p$. Thus, we can partition Z_p into cycles that differ from each other by boundaries through the quotient space

$$H_p = Z_p / B_p,$$

which is called the p -th homology group. The p -th Betti number β_p counts the number of algebraically independent p -cycles, i.e.,

$$\beta_p = \text{rank} H_p = \text{rank} Z_p - \text{rank} B_p.$$

Graph G is 1-skeleton [52], Betti numbers $\beta_0(G)$ and $\beta_1(G)$ counts the number of connected components (0-cycles) and number of loops (1-cycles) respectively.

Birth-death decomposition The graph filtration of G is defined as a sequence of nested binary networks [53,35]:

$$G_{\epsilon_0} \supset G_{\epsilon_1} \supset \dots \supset G_{\epsilon_k}$$

where $\epsilon_0 < \epsilon_1 < \dots < \epsilon_k$ are the filtration values. These nested graphs are usually obtained by slicing G into a series of binary graphs using the sorted edge weights as thresholds.

Although there are many possible graph filtrations over the different choice of threshold values, the best practice is to use edge weights as filtration values which renders the graph filtration to be unique [35,31].

For $\epsilon_0 = -\infty$, G_{ϵ_0} is a complete graph while for $\epsilon_k = \infty$, G_{ϵ_k} is the node set V . The graph filtration is built from a complete network G_{ϵ_0} by sequentially removing one edge at a time till we reach the node set G_{ϵ_k} . During the graph filtration, as we delete one edge, the number of connected components (0-cycles) increases monotonically while the number of loops (1-cycles) decrease at most by one [54]. The birth and death of k -cycles during the process of filtration is quantified using *persistence*, which is the duration of filtration values from birth to death. The persistence is usually represented as 1D intervals as persistent barcode (PB) [55,56,34] or 2D scatter points as a persistent diagram (PD) [57]. These barcodes or diagrams are referred to as topological signatures of the data.

Since G_{ϵ_0} is a complete graph, a single connected component, we associate its birth time to be $-\infty$ in the graph filtration. Owing to the monotonicity of β_0 [54], the connected components that are born never die. Thus, we associate its death values of ∞ for every connected component. Ignoring the first birth value corresponding to the complete graph at $-\infty$, the total number of birth values of connected components is then

$$\mathcal{P} = \beta_0(G_\infty) - 1 = p - 1. \quad (3)$$

The 0D barcode corresponding to 0-cycles consists of a set of increasing birth values

$$B(G) = b_1 < b_2 < \dots < b_{\mathcal{P}}.$$

In a graph, all the loops (1-cycles) are considered born at $-\infty$. Starting with complete graph $G_{-\infty}$ with p nodes, there are $q = p(p-1)/2$ unique edge weights. During the graph filtration, when an edge is deleted, either a new connected component is born or a loop dies. But these events are disjoint and does not happen at the same time [54]. When the loop dies, we associate it with the edge weight as the death value. Let \mathcal{Q} be the total number of death values of 1-cycles. Then the total number of edges is equivalent to

$$q = \mathcal{P} + \mathcal{Q}.$$

Thus, we have $\mathcal{Q} = (p-1)(p-2)/2$ number of death values and 1D barcode contains only a set of increasing death values written as

$$D(G) = d_1 < d_2 < \dots < d_{\mathcal{Q}}.$$

In essence, the graph filtration ensures that deleting edge in the network G must result in either the birth of a connected component or the death of a cycle. The birth of a component and the death of a cycle cannot occur at the same instant. This is more formally stated as [54]:

Theorem 1 (Birth-death decomposition). *The set of 0D birth values $B(G)$ and 1D death values $D(G)$ partition the edge weight set W such that $W = B(G) \cup D(G)$ with $B(G) \cap D(G) = \emptyset$. The cardinalities of $B(G)$ and $D(G)$ are $p-1$ and $(p-1)(p-2)/2$ respectively.*

Figure 2 displays a toy example of the birth-death decomposition. Theorem 1 plays a central role in the computation of persistent barcodes and the formulation of the proposed 1-cycle identification using the Hodge Laplacian.

Numerical implementation In the graph filtration, we only need to compute the birth values of the connected components and the death values for the cycles. The birth values are easily computed using the maximum spanning tree (MST). Given a weighted graph G ,

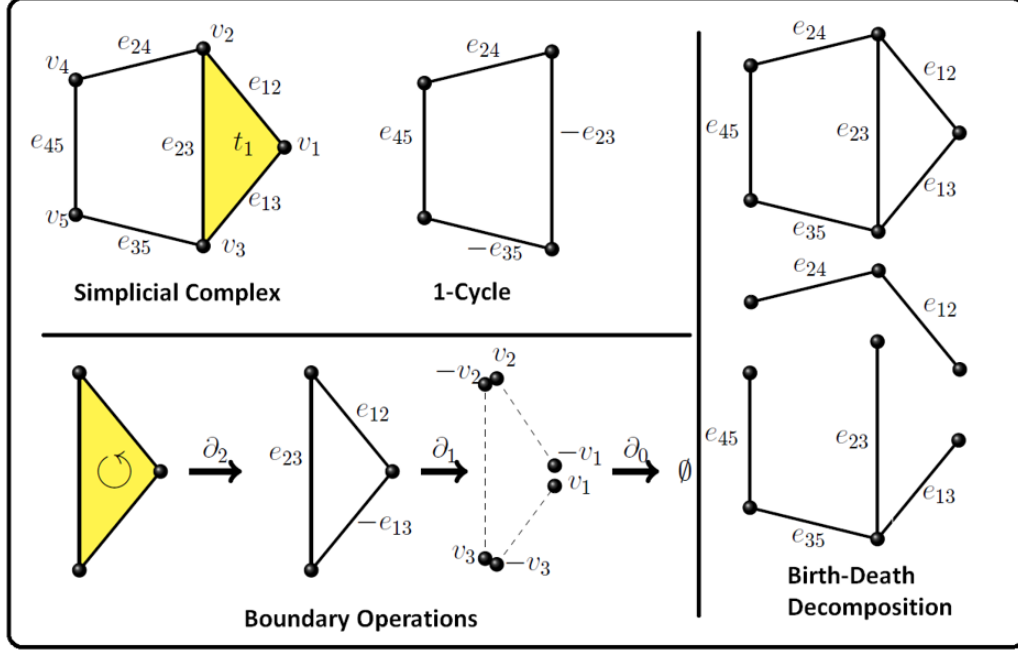


Fig. 2: Top left: A simplicial complex with five vertices (0-simplex), six edges (1-simplex) and a triangle (2-simplex). The triangle is represented by $t_1 = [v_1, v_2, v_3]$ with a filled-in face (colored yellow). Bottom left: A sequence of boundary operations applied to t_1 . After boundary operation ∂_2 , we get the 1-simplices $[v_1, v_2] + [v_2, v_3] - [v_1, v_3] = e_{12} + e_{23} - e_{13}$ which is the boundary of the triangle [36,30]. Right: A graph (G) is decomposed into death set $D(G)$ with edges $[e_{12}, e_{24}]$ and birth set $B(G)$ with edges $[e_{13}, e_{23}, e_{35}, e_{45}]$.

computing the set of 0D birth values $B(G)$ of the connected component is equivalent to the finding MST of G [54]. The identification of MST is based on Kruskal's or Prim's algorithms [34]. Once $B(G)$ is computed, the set of 1D death values $D(G)$ is simply given as the rest of the remaining edge weights that are not part of MST from Theorem 1. Thus, the 1D barcodes for 0- and 1-cycles can be computed efficiently in $\mathcal{O}(q \log p)$.

Wasserstein distance on graphs Since the barcodes embed the topological information about the network, the topological similarity or dissimilarity between the networks can be inferred from the differences between barcodes [58]. The Wasserstein distance is a metric that is often used to quantify the underlying differences in the barcodes [59,54]. Let $\Omega = (V^\Omega, w^\Omega)$ and $\Psi = (V^\Psi, w^\Psi)$ be two given networks with p nodes. Their persistent diagrams denoted as P_Ω and P_Ψ are expressed in terms of scatter points as

$$x_1 = (b_1^\Omega, d_1^\Omega), \dots, x_q = (b_q^\Omega, d_q^\Omega)$$

and

$$y_1 = (b_1^\Psi, d_1^\Psi), \dots, y_q = (b_q^\Psi, d_q^\Psi)$$

respectively. The 2- *Wasserstein distance* \mathcal{D}_W between two probability distributions $X \sim f_\Omega$ and $Y \sim f_\Psi$, is defined as

$$\mathcal{D}(X, Y) = \left(\inf \mathbb{E} \|X - Y\|^2 \right)^{1/2}, \quad (4)$$

where the infimum is taken over every possible joint distributions between X and Y . If we assign empirical distributions to the persistent diagrams P_Ω and P_Ψ using the Dirac-delta

functions we get, $f_\Omega(x) = \frac{1}{Q} \sum_{i=1}^Q \delta(x - x_i)$ and $f_\Psi(y) = \frac{1}{Q} \sum_{i=1}^Q \delta(y - y_i)$ then we can show that the 2-Wasserstein distance on persistent diagrams is given by

$$\mathcal{D}(P_\Omega, P_\Psi) = \inf_{\tau: P_\Omega \rightarrow P_\Psi} \left(\sum_{x \in P_\Omega} \|x - \tau(x)\|^2 \right)^{1/2}$$

over every possible bijection τ between P_Ω and P_Ψ [59].

The Wasserstein distance computation for scatter points relies on solving the associated assignment problem, using the Kuhn-Munkres approach and Hungarian algorithm [60,61,62]. These methods are computationally complex and takes $\mathcal{O}(Q^3)$ running time [63]. However, for graph filtration, the distance can be computed in $\mathcal{O}(Q \log Q)$ by simply matching the order statistics on birth or death values [64,54]. Intuitively, $\mathcal{D}(P_\Omega, P_\Psi)$ quantifies the optimal expected cost of transporting points generated from f_Ω to those generated from f_Ψ [65,66]. For graph filtrations, since persistent diagrams are 1D scatter points, the bijection τ is simply given by matching sorted scatter points [54]:

Theorem 2. *2-Wasserstein distance between the 0D persistent diagrams for graph filtration is given by*

$$\mathcal{D}_0(P_\Omega, P_\Psi) = \left[\sum_{i=1}^q (b_{(i)}^\Omega - b_{(i)}^\Psi)^2 \right]^{1/2},$$

where $b_{(i)}^\Omega$ and $b_{(i)}^\Psi$ are the i -th smallest birth values associated with 0-cycles (connected components). 2-Wasserstein distance between the 1D persistent diagrams for graph filtration is given by

$$\mathcal{D}_1(P_\Omega, P_\Psi) = \left[\sum_{i=1}^q (d_{(i)}^\Omega - d_{(i)}^\Psi)^2 \right]^{1/2},$$

where $d_{(i)}^\Omega$ and $d_{(i)}^\Psi$ are the i -th smallest death values associated with 1-cycles (loops).

In this study, we focus on the 2-Wasserstein distance between loops.

2.2 Hodge Laplacian over simplicial complexes

The Hodge Laplacian generalizes the usual graph Laplacian for nodes (0-simplices) to p -simplices. The Laplacian matrix \mathcal{L}_0 for a graph is given by $\mathcal{L}_0 = D - A$. The D is the degree matrix and A is the adjacency matrix. In general, a higher-dimensional Laplacian can be defined for each dimension p using two matrices that perform the role of upper and lower adjacency matrices:

$$\mathcal{L}_p = \mathcal{L}_p^U + \mathcal{L}_p^L$$

where \mathcal{L}_p^U and \mathcal{L}_p^L are called the upper and lower adjacency Laplacians [19].

Hodge Laplacian The higher dimensional Laplacian \mathcal{L}_p is usually referred to as the Hodge Laplacian or the p -Laplacian that connects the p -simplices with their adjacent $(p+1)$ -(upper adjacency) and $(p-1)$ -simplices (lower adjacency). To enable efficient computation of Hodge Laplacian, we represent the boundary operator ∂_p using the boundary matrix \mathcal{B}_p defined as [67,68]

$$(\mathcal{B}_p)_{ij} = \begin{cases} 1, & \text{if } \sigma_{p-1}^i \subset \sigma_p^j \text{ and } \sigma_{p-1}^i \sim \sigma_k^j \\ -1, & \text{if } \sigma_{p-1}^i \subset \sigma_p^j \text{ and } \sigma_{p-1}^i \approx \sigma_k^j, \\ 0, & \text{if } \sigma_{p-1}^i \not\subset \sigma_p^j \end{cases}, \quad (5)$$

where σ_{p-1}^i is the i -th $(p-1)$ -simplex and σ_p^j is the j -th p -simplex. Notations \sim and \approx denote similar (positive) and dissimilar (negative) orientations respectively.

Then the p -th Hodge Laplacian matrix \mathcal{L}_p of K is defined using the boundary matrices, which is the matrix form of the boundary operators:

$$\mathcal{L}_p = \mathcal{B}_p^T \mathcal{B}_p + \mathcal{B}_{p+1} \mathcal{B}_{p+1}^T. \quad (6)$$

More specifically, \mathcal{L}_p is viewed as the sum of the Laplacians composed of boundary matrices from the lower dimensional simplices [69,70,71,72]: $\mathcal{L}_p^L = \mathcal{B}_p^T \mathcal{B}_p$ and upper dimensional simplices $\mathcal{L}_p^U = \mathcal{B}_{p+1} \mathcal{B}_{p+1}^T$. Since $\mathcal{B}_0 = 0$, the Hodge Laplacian for a 1-skeleton is $\mathcal{L}_0 = \mathcal{B}_1 \mathcal{B}_1^T$, which is popularly referred as the graph Laplacian [48]. The boundary matrix \mathcal{B}_1 which relates nodes to edges is commonly referred as incidence matrix in graph theory. Further, we also have $\mathcal{L}_1 = \mathcal{B}_1^T \mathcal{B}_1 + \mathcal{B}_2 \mathcal{B}_2^T$. In case of a 1-skeleton, Since there is only 0-simplex and 1-simplex, the boundary matrix $\mathcal{B}_2 = 0$, thus the second term in the Hodge Laplacian \mathcal{L}_1 vanishes and we have

$$\mathcal{L}_1 = \mathcal{L}_1^L = \mathcal{B}_1^T \mathcal{B}_1.$$

The computation of a p -th Hodge-Laplacian requires the construction of p -skeletons and the boundary matrices from $(p-1)$ -skeletons in a hierarchical fashion. The technical details on the computation of p -skeleton can be found in [73]. In brain network studies, brain networks are usually expressed as a connectivity matrix which allows us to directly compute 1-skeletons. In this study, we only use upto 2-skeletons which contain the 0-simplices (nodes), 1-simplices (edges) and the 2-simplices (triangles). A 2-skeleton is built sequentially starting from with 0-simplices and then the 1-simplices are added to build a 1-skeleton, followed by the addition of 2-simplices to form a 2-skeleton in a hierarchical fashion.

Example 1 We illustrate Hodge Laplacian computation using simplicial complex K_1 in Figure 2. The simplicial complex K_1 consists of node set $V = \{v_1, v_2, v_3, v_4, v_5\}$ connected by edge set $E = \{e_{12}, e_{13}, e_{23}, e_{24}, e_{35}, e_{45}\}$ with $e_{ij} = [v_i, v_j] = v_j - v_i$ and triangle $t_1 = [v_1, v_2, v_3]$. The boundary matrices \mathcal{B}_1 and \mathcal{B}_2 are given by

$$\mathcal{B}_1 = \begin{matrix} v_1 \\ v_2 \\ v_3 \\ v_4 \\ v_5 \end{matrix} \begin{pmatrix} e_{12} & e_{13} & e_{23} & e_{24} & e_{35} & e_{45} \\ -1 & -1 & 0 & 0 & 0 & 0 \\ 1 & 0 & -1 & -1 & 0 & 0 \\ 0 & 1 & 1 & 0 & -1 & 0 \\ 0 & 0 & 0 & 1 & 0 & -1 \\ 0 & 0 & 0 & 0 & 1 & 1 \end{pmatrix} \quad \mathcal{B}_2 = \begin{matrix} t_1 \\ e_{12} \\ e_{13} \\ e_{23} \\ e_{24} \\ e_{35} \\ e_{45} \end{matrix} \begin{pmatrix} 1 \\ -1 \\ 1 \\ 0 \\ 0 \\ 0 \end{pmatrix}. \quad (7)$$

The boundary matrix \mathcal{B}_1 maps the nodes (0-simplex) to edges (1-simplex) and \mathcal{B}_2 maps the edges (1-simplex) to triangle (2-simplex). In this example, we have six edges and a triangle and hence the size of \mathcal{B}_2 is 6×1 . Subsequently, the Hodge Laplacian matrix \mathcal{L}_1 is given by $\mathcal{L}_1 = \mathcal{B}_1^T \mathcal{B}_1 + \mathcal{B}_2 \mathcal{B}_2^T$:

$$\mathcal{L}_1 = \begin{pmatrix} 3 & 0 & 0 & -1 & 0 & 0 \\ 0 & 3 & 0 & 0 & -1 & 0 \\ 0 & 0 & 3 & 1 & -1 & 0 \\ -1 & 0 & 1 & 2 & 0 & -1 \\ 0 & -1 & -1 & 0 & 2 & 1 \\ 0 & 0 & 0 & -1 & 1 & 2 \end{pmatrix}.$$

2.3 Algebraic representation of 1-cycles

The spectral decomposition of Hodge Laplacian is performed to identify p -cycles of the underlying network [69,48]. The p -th homology group H_p is a kernel of Hodge Laplacian \mathcal{L}_p [69,36,74,68], i.e.,

$$H_p = \ker \mathcal{L}_p.$$

The eigenvectors with zero eigenvalues of \mathcal{L}_p span the kernel space of \mathcal{L}_p . Thus, numerically we find the eigenvectors corresponding to the zero eigenvalues of \mathcal{L}_p . We first solve

$$\mathcal{L}_p \mathbf{U}_p = \Lambda_p \mathbf{U}_p$$

where, Λ_p is a diagonal matrix of eigenvalues and \mathbf{U}_p is a matrix of eigenvectors. The multiplicity of the zero eigenvalue of Hodge Laplacian \mathcal{L}_p is the Betti number β_p , the rank of the kernel space of \mathcal{L}_p . This is related to the algebraic connectivity and generalizes from the well known fact that the number of zero eigenvalues of the graph Laplacian is the number of connected components [48]. Similarly, the number of zero eigenvalues of the \mathcal{L}_0 , \mathcal{L}_1 and \mathcal{L}_2 matrix corresponds to the number of 0-cycles (connected components), 1-cycles (closed loops) and 2-cycles (voids or cavities) respectively. Since the eigenvectors corresponding to the zero eigenvalues are related to the homology generators [75], we represent a 1-cycle using the coefficients of the eigenvectors. Let $A = (a_{l(i,j),m})$ be the collection the columns of \mathbf{U}_1 that corresponds to the zero eigenvalues, where $a_{l(i,j),m}$ corresponds to edge e_{ij} . The size of A_1 is $q \times \beta_1$ with Betti number β_1 . Each column of A corresponds to 1-cycles. The m -th 1-cycle \mathcal{C}^m can be represented as

$$\mathcal{C}^m = \sum_{e_{ij} \in E} a_{l(i,j),m} e_{ij}. \quad (8)$$

\mathcal{C}^m can be represented as a vector by putting coefficient $a_{l(i,j),m}$ into the corresponding position in the lexicographically ordered edge set $[e_{12}, e_{13}, \dots, e_{23}, e_{24}, \dots, e_{q-1,q}]^T$. Following Example 1 (Figure 2), the eigendecomposition of \mathcal{L}_1 results in \mathbf{U}_1 and Λ_1 :

$$\Lambda_1 = \begin{pmatrix} \mathbf{0.00} & 0 & 0 & 0 & 0 & 0 \\ 0 & 1.38 & 0 & 0 & 0 & 0 \\ 0 & 0 & 2.38 & 0 & 0 & 0 \\ 0 & 0 & 0 & 3.00 & 0 & 0 \\ 0 & 0 & 0 & 0 & 3.62 & 0 \\ 0 & 0 & 0 & 0 & 0 & 4.62 \end{pmatrix}$$

and

$$\mathbf{U}_1 = \begin{pmatrix} \mathbf{-0.17} & 0.37 & -0.24 & -0.57 & -0.60 & -0.28 \\ \mathbf{0.17} & 0.37 & 0.24 & 0.57 & -0.60 & 0.28 \\ \mathbf{0.35} & 0.00 & 0.48 & -0.57 & 0.00 & 0.56 \\ \mathbf{-0.52} & 0.60 & -0.15 & 0.00 & 0.37 & 0.45 \\ \mathbf{0.52} & 0.60 & 0.15 & 0.00 & 0.37 & -0.45 \\ \mathbf{-0.52} & 0.00 & 0.78 & 0.00 & 0.00 & -0.35 \end{pmatrix}.$$

The bold numbers represent the eigenvector corresponding to the zero eigenvalue. In this example, the 1-cycle is represented as

$$\mathcal{C}^1 = -0.17e_{12} + 0.17e_{13} + 0.35e_{23} - 0.52e_{24} + 0.52e_{35} - 0.52e_{45}.$$

Since there is no preference in sign, we can also have $-\mathcal{C}^1$ as the representation as well. However, since all the edges have some weights, it is difficult to determine which edges belong to 1-cycle in this particular simplex.

Example 2 Consider a simplicial complex K_2 made of node set $V = \{v_1, v_2, v_3, v_4, v_5\}$ connected by edge set $E = \{e_{12}, e_{23}, e_{24}, e_{35}, e_{45}\}$ (Figure 3-right). Here, we remove the edge e_{13} such that the triangle is destroyed and only one cycle is retained in the network from the simplicial complex K_1 from Example 1. While K_1 has a triangle, K_2 has no triangle and only one 1-cycle. We now follow the same procedure carried out for K_1 . The boundary matrix \mathcal{B}_1 and the Hodge Laplacian \mathcal{L}_1 are given by

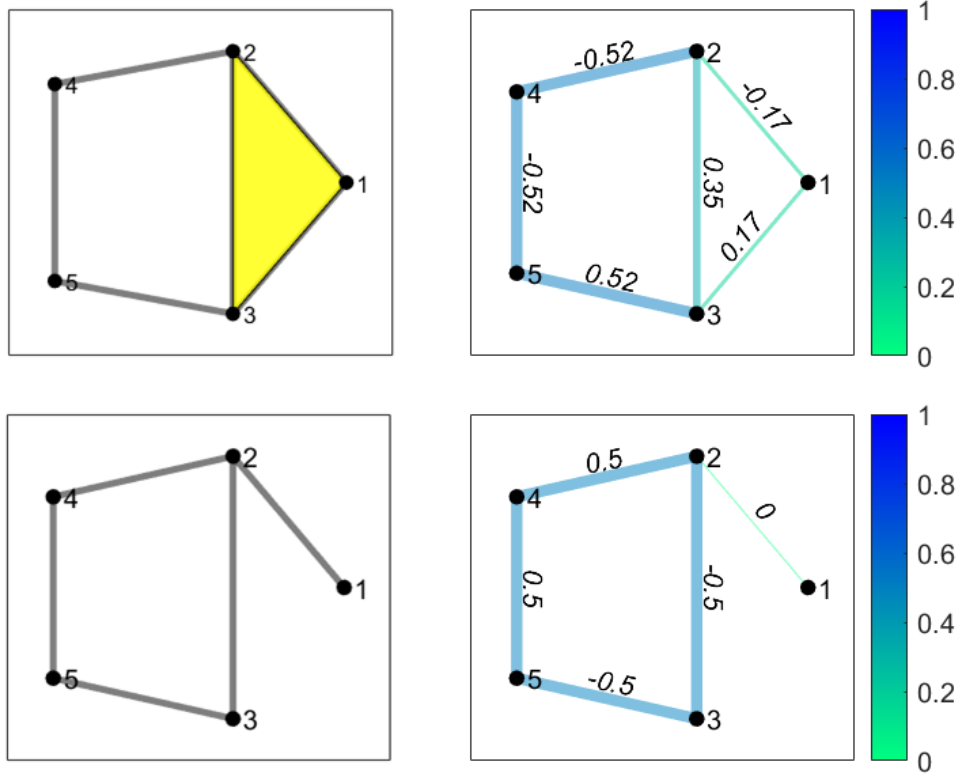


Fig. 3: Top-left: A 2-skeleton representation network in Example 1 made of five vertices connected by six edges. Top-Right: The 1-cycle is formed by the vertices v_2, v_4, v_5, v_3 is identified by the eigen decomposition of the Hodge-Laplacian (\mathcal{L}_1). The edge colors indicate the absolute value of coefficients of the cycle representation C^1 . Bottom-left: 1-skeleton representation of the network in Example 2 made of five vertices connected by five edges. Bottom-right: The 1-cycle identified along with the edges that constitute the cycle.

$$\mathcal{B}_1 = \begin{matrix} v_1 \\ v_2 \\ v_3 \\ v_4 \\ v_5 \end{matrix} \begin{pmatrix} e_{12} & e_{23} & e_{24} & e_{35} & e_{45} \\ -1 & 0 & 0 & 0 & 0 \\ 1 & -1 & -1 & 0 & 0 \\ 0 & 1 & 0 & -1 & 0 \\ 0 & 0 & 1 & 0 & -1 \\ 0 & 0 & 0 & 1 & 1 \end{pmatrix}, \mathcal{L}_1 = \begin{pmatrix} 2 & -1 & -1 & 0 & 0 \\ -1 & 2 & 1 & -1 & 0 \\ -1 & 1 & 2 & 0 & -1 \\ 0 & -1 & 0 & 2 & 1 \\ 0 & 0 & -1 & 1 & 2 \end{pmatrix}.$$

The eigen decomposition is performed on the Hodge-Laplacian \mathcal{L}_1 results in the eigenvalues $[0.00, 0.83, 2.00, 2.69, 4.48]$ and the eigenvector corresponding to the zero eigenvalue is obtained as $[0.00, 0.50, -0.50, 0.50, -0.50]$. Further, the 1-cycle is represented as

$$C^1 = 0.5e_{23} - 0.5e_{24} + 0.5e_{35} - 0.5e_{45}.$$

Figure 3-bottom left is a 1-skeleton representation for this example. It is a graph since there are no higher order simplices beyond nodes and edges. In such a case, we obtain 1-cycle representation as seen in Figure 3-bottom right with only the edges that constitute the 1-cycle. This example illustrates that in order to identify and extract the 1-cycles, we need to break down the graph into series of subgraph such that each subgraph contains only one 1-cycle.

Computation of 1-cycle basis The representation (8) uses all the edges representing a 1-cycle. Even the edges that are not a part of a cycle are used in the representation. This has been the main limitation of using Hodge Laplacian in identifying 1-cycles in the past [36]. In the proposed method, we split the graph into a series of subgraphs such that each subgraph has only one 1-cycle.

Recall that the graph filtration partitions the edges in a given network uniquely into the birth and death sets. While the edges in the birth set are responsible for creating components, the edges in the death set accounts for destroying cycles. The edges in the birth set forms the maximums spanning tree (MST) with no cycles. Upon add an edge from the death set to MST a 1-cycle is formed. The process is repeated sequentially till we use up all the edges in the death set. We claim the resulting 1-cycles form a basis.

Theorem 3. *Let $M(G) = (V, T)$ be the MST of graph G . When an edge d_k from the death set $D(G)$ is added to the MST, 1-cycle \mathcal{C}^k is born. The collection of cycles $\mathcal{C}^1, \dots, \mathcal{C}^Q$ spans $\ker \mathcal{L}_p$.*

Proof. Let E_k be the edge set of the cycle \mathcal{C}^k . Since E_k and E_l differ at least by an edge d_k and d_l , they are algebraically independent. Hence, all the cycles E_1, \dots, E_Q are independent from each other. Since there should be Q number of independent cycles in the p -th Homology group $H_p = \ker \mathcal{L}_p$, they form a basis. \square

The 1-cycles can now be sequentially extracted by using the Hodge Laplacian of the subgraph $G_k = (V, T \cup \{d_k\})$, which contains a cycle \mathcal{C}^k . We get exactly one eigenvector corresponding to the zero eigenvalue. The entries of eigenvector will be all zero on the edges that are not part of cycle. Thus, we can represent 1-cycle \mathcal{C}^k only using edges that contribute to the cycle:

$$\mathcal{C}^k = \sum_{e_{ij} \in E_k} a_{l(i,j),k} e_{ij}. \quad (9)$$

Here $a_{l(i,j),k}$ is the entries of eigenvector of the Hodge Laplacian corresponding to edge e_{ij} . The representation (9) contains only the edges that form the cycle. All other terms are zero. Thus, \mathcal{C}^k can be represented as vectors by putting $a_{l(i,j),k}$ into the corresponding position in the vectorized edge set $[e_{12}, e_{13}, \dots, e_{23}, e_{24}, \dots, e_{q-1,q}]^T$. Subsequently, all the 1-cycle basis $\mathcal{C}^1, \dots, \mathcal{C}^Q$ can be systematically extracted and efficiently stored as a sparse matrix. Since $\mathcal{C}^1, \dots, \mathcal{C}^Q$ forms a basis, any cycle in the graph can be represented as a linear combination $\sum_{j=1}^Q \alpha_j \mathcal{C}^j$.

2.4 Statistical analysis on topological features of cycles

We present how to use topological features such as death values and length of cycles in analyzing collection of brain networks. Let $\Omega = \{\Omega_1, \dots, \Omega_m\}$ and $\Psi = \{\Psi_1, \dots, \Psi_n\}$ be a collection of m and n complete networks each consisting of p number of nodes. There are exactly $Q = (p-1)(p-2)/2$ number of cycles in each network. We are interested in developing new statistical inference procedures testing the topological equivalence of two groups of networks Ω and Ψ .

Inference on death values We test the topological equivalence of two groups of networks Ω and Ψ using the Wasserstein distances within groups \mathcal{L}_W and between groups \mathcal{L}_B [54]:

$$\mathcal{L}_W = \frac{\sum_{i < j} \mathcal{D}_1(\Omega_i, \Omega_j) + \sum_{i < j} \mathcal{D}_1(\Psi_i, \Psi_j)}{\binom{m}{2} + \binom{n}{2}} \quad \text{and} \quad \mathcal{L}_B = \frac{\sum_{i=1}^m \sum_{j=1}^n \mathcal{D}_1(\Omega_i, \Psi_j)}{mn}.$$

Note we are only using the Wasserstein distance between cycles, which are computed as the squared sum of sorted death values. Then we use the ratio $\mathcal{L}_{B/W} = \mathcal{L}_B / \mathcal{L}_W$ as the test

statistic. If the two groups are close, \mathfrak{L}_B becomes small while \mathfrak{L}_W becomes large. Thus the ratio $\mathfrak{L}_{B/W}$ can be used to as test statistic.

Since the probability distribution of $\mathfrak{L}_{B/W}$ is unknown, we used the permutation test [76,77,78,79,80]. For large sample sizes m and n as in our study, the permutation test will be computationally costly. The total number of permutations when $m = n$ is given asymptotically by Stirling's formula [81]

$$\binom{2m}{m} \sim \frac{4^m}{\sqrt{\pi m}}.$$

The number of permutations *exponentially* increases as the sample size increases, and thus it is impractical to generate every possible permutation. Thus, we adapted for the scalable *transposition test* that sequentially update the test statistic over transpositions [82,83,54].

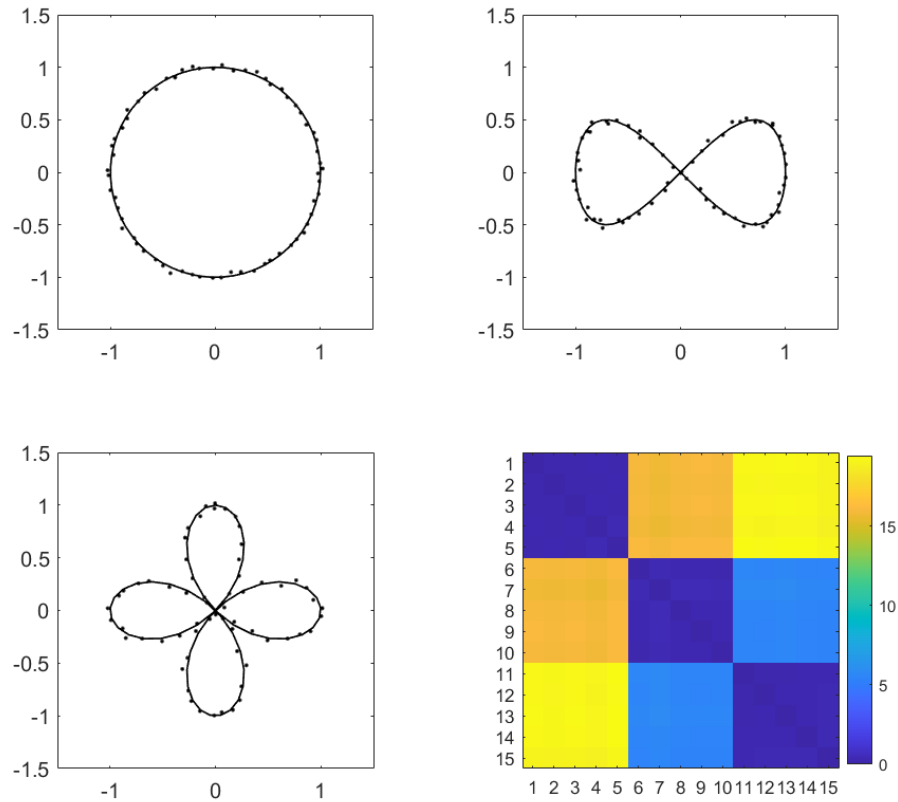


Fig. 4: The three types of cycles with different topology: circle (1-loop), lemniscate (2-loops), quadrifolium (4-loops) used in the simulation study. The Gaussian noise $\mathcal{N}(0, 0.02^2)$ is added to the coordinates of curves. Bottom right: the pairwise Wasserstein distance matrix computed using the death values of the 1-cycles on 5 networks in each group. The Wasserstein distance matrix shows clear clustering pattern demonstrating the method can easily discriminate networks of different 1D topology.

Unlike the permutation test that shuffles all the networks, the permutation test only shuffles one network per group. Computing the statistic $\mathfrak{L}_{B/W}$ over each permutation requires the recomputation of the Wasserstein distance. Instead, we perform the transposition

of swapping only one network per group and setting up iteration of how the test statistic change over the transposition. Let π_{kl} be the transposition of the k -th network in Ω and the l -th network in Ψ :

$$\begin{aligned}\pi_{kl}(\Omega) &= \{\Omega_1, \dots, \Omega_{k-1}, \Psi_l, \Omega_{k+1}, \dots, \Omega_m\}, \\ \pi_{kl}(\Psi) &= \{\Psi_1, \dots, \Psi_{l-1}, \Omega_k, \Psi_{l+1}, \dots, \Psi_n\}.\end{aligned}$$

Over the transposition π_{kl} , the within and between group distances are updated as

$$\begin{aligned}\mathfrak{L}_W(\pi_{kl}(\Omega), \pi_{kl}(\Psi)) &= \mathfrak{L}_W(\Omega, \Psi) + \Delta\mathfrak{L}_W, \\ \mathfrak{L}_B(\pi_{kl}(\Omega), \pi_{kl}(\Psi)) &= \mathfrak{L}_B(\Omega, \Psi) + \Delta\mathfrak{L}_B,\end{aligned}$$

where the incremental changes $\Delta\mathfrak{L}_W$ and $\Delta\mathfrak{L}_B$ are given as the sum of difference of death values involved in the transpositions [54]. The algorithm recycles the previous computation of \mathfrak{L}_B and \mathfrak{L}_W . Instead of recomputing all $n \times m$ terms in as in the standard permutations, we only use $2(n+m)$ terms drastically reducing the run time in computing each permutation. Thus, more permutations can be generated given the same amount of run-time, which speed up the convergence of transposition procedure. In this study, we generate the test statistics with sufficiently large number of 500000 random transpositions while injecting a random permutation for every 500 transpositions. The intermix of transpositions and permutations has the effect of speeding up the convergence [82].

Inference on length Another obvious feature of a 1-cycle is its length. So we investigated if the length of a cycle can be used as a discriminating feature. We defined the length of a 1-cycle as as the number of edges in the cycle. Let

$$u_1^i \leq u_2^i \leq \dots \leq u_{\mathcal{Q}}^i$$

be the sorted length of 1-cycles in Ω_i . The average sorted lengths across subjects are given by

$$\bar{u}_1 \leq \bar{u}_2 \leq \dots \leq \bar{u}_{\mathcal{Q}},$$

where

$$\bar{u}_j = \frac{u_j^1 + u_j^2 + \dots + u_j^m}{m} \quad (10)$$

is the average length of j -th cycles in group Ω . Similarly we sort the length of 1-cycles in Ψ_i as

$$v_1^i \leq v_2^i \leq \dots \leq v_{\mathcal{Q}}^i$$

and obtain the average sorted lengths across subjects

$$\bar{v}_1 \leq \bar{v}_2 \leq \dots \leq \bar{v}_{\mathcal{Q}},$$

Subsequently, we use the maxim difference

$$\mathfrak{L}(\Omega, \Psi) = \max_{1 \leq j \leq \mathcal{Q}} |\bar{u}_j - \bar{v}_j| \quad (11)$$

as the test statistic in discriminating between two groups of networks. The statistical significance is determined using the standard permutation test with 500000 permutations. The test statistic do not yield the transposition type of fast computation.

Network clustering using Wasserstein distance on death values It is possible to cluster a collection of networks purely based on cycles present in the networks. Using the Wasserstein distance on cycles, we cluster collection of networks $A_1, A_2 \dots A_n$ into k clusters $A_1, A_2 \dots A_k$ such that:

$$\cup_{i=1}^k A_i = \{A_1, \dots, A_n\}, \quad A_i \cap A_j = \emptyset \quad (i \neq j)$$

Let $X_i = (d_{(1)}^{A_i}, d_{(2)}^{A_i} \dots, d_{(Q)}^{A_i})^T$ be the vector of Q sorted death values of network A_i :

$$d_{(1)}^{A_i} < d_{(2)}^{A_i} < \dots < d_{(Q)}^{A_i}.$$

The 1D Wasserstein distance D_1 between two cycles is given by:

$$D_1^2(A_i, A_j) = \sum_{k=1}^Q (d_{(k)}^{A_i} - d_{(k)}^{A_j})^2 = d(X_i, X_j)^2,$$

where $d^2(X_i, X_j) = (X_i - X_j)^T(X_i - X_j)$ is the 2-norm between vectors X_i and X_j . Note that the sorted vector X_i is a point in the $(q+1)$ -simplex (q -dimensional tetrahedron) given by

$$\mathcal{T} = \{(x_1, x_2, \dots, x_{q+1}) | x_1 < x_2 < \dots < x_{q+1}\} \subset \mathbb{R}^{q+1}.$$

Hence, the Wasserstein distance is equivalent to Euclidean distance in the q -dimensional convex set \mathcal{T} . Any operation on the Wasserstein distance can be done as if it is Euclidean distance within \mathcal{T} .

Define the Wasserstein mean of cluster A_j as a network \bar{A}_j satisfying

$$\bar{A}_j = \arg \min_{A} \sum_{A_i \in A_j} D_1(A, A_i).$$

The within-cluster Wasserstein distance is given by:

$$l_W(A_1, \dots, A_k) = \sum_{j=1}^k \sum_{A \in A_j} D_1^2(A, \bar{A}_j) \quad (12)$$

The optimal cluster is found by minimizing l_W over every possible clusters A_1, \dots, A_k . Just like Fréchet mean, the mean network is not unique in a geometric sense but only unique in a topological sense [84,85,86,87]. Even though the cluster mean is not uniquely defined, the Wasserstein distance itself is uniquely defined. Thus, we can still be able to minimize (12) by replacing the Wasserstein distance with the 2-norm between sorted vectors of death values in \mathcal{T} . This is then equivalent to k -means clustering restricted to the convex set \mathcal{T} . The convergence of Wasserstein clustering is then the direct consequence of the convergence of k -means clustering, which always converges in such a convex space.

Different choice of initial cluster centers may lead to different results. So the algorithm may stuck in a local minimum and may not converge to global minimum. Thus, in actual numerical implementation, we used different initializations of centers. Then picked the best one clustering results with the smallest within cluster distance l_W .

2.5 Spectral geometry approach of using 1-cycle basis

So far we investigated how to use topological features of cycles in statistical inference and clustering. In this section, we present the spectral geometry approach of using 1-cycle basis in modeling brain connectivity. Brain images are often denoised to increase the signal-to-noise ratio (SNR) and enhance statistical sensitivity. Denoising induces many nice statistical properties such as variance reduction and improves sensitivity [88,89]. Brain connectivity matrices are noisy so it is necessary to denoise the matrices as well. We extend the concept of heat diffusion defined on brain surfaces [88,89] to simplicial complexes. We propose to perform heat diffusion over 1-simplices (edges) using the eigenvectors of Hodge Laplacian as follows.

Heat diffusion on connectivity matrices Let \mathcal{K} be a collection of 1-simplices with cardinality $|\mathcal{K}|$. Let f be the initial observed data defined over \mathcal{K} . For instance, f can be the vectorization of upper triangle of edge weight matrix $w = (w_{ij})$. We will perform heat diffusion smoothing over \mathcal{K} :

Theorem 4. *The unique solution to diffusion equation over \mathcal{K}*

$$\frac{\partial g(t)}{\partial t} = \mathcal{L}_1 g(t) \quad (13)$$

with initial condition $g(t=0) = f$ is given by

$$g(t) = \sum_{j=0}^{|\mathcal{K}|-1} e^{-\lambda_j t} f_j \psi_j \quad (14)$$

where λ_j and ψ_j are the j -th eigenvalue and eigenvector of the Laplacian matrix \mathcal{L}_1 , and $f_j = f^T \psi_j$.

Unlike existing heat diffusion methods which defines the smoothing over nodes, we are defining along edges [88,89]. This smoothing process is illustrated in Figure 5. Starting with the original network data (bandwidth of 0), as the bandwidth increases, the network gradient decreases reducing high frequency noise.

We can show that the variance across subjects at each edge is reduced after smoothing. If we denote $\mathbb{V}_i f$ to be the variance of functional measurement f across subject at the i -th edge, we can algebraically show that

$$\mathbb{V}_i g(t) \leq \mathbb{V}_i f$$

for all t . After heat diffusion smoothing, the variance will be reduced and statistical sensitivity of group discrimination will increase. This variance reduction property is demonstrated in Figure 6. We smoothed the brain networks of 400 subjects with three different smoothing bandwidths 0.001, 0.005, and 0.01. We observe that the variation of the smoothed data across all edges is consistently less compared to the initial non-smoothed data. This reduced variation is as a result of the heat diffusion smoothing removing high frequency noise, and hence has the effect of increasing statistical sensitivity.

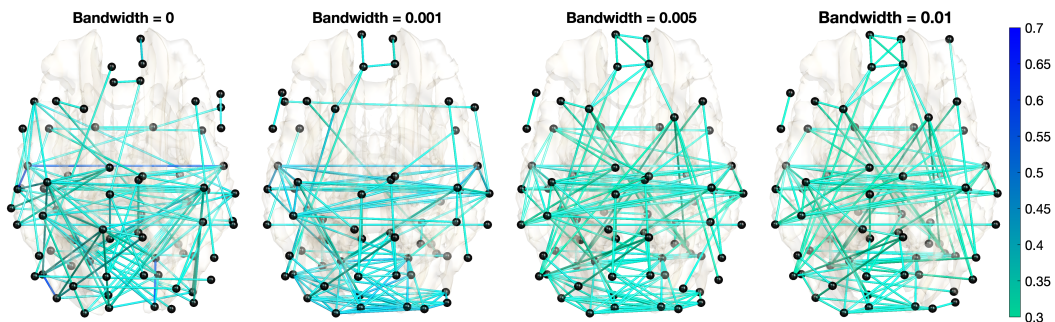


Fig. 5: The smoothed connectivity maps, thresholded for better visualization. The very left represents the initial edge data with some potential high frequency noise influencing the blue-gradient edges. After smoothing with a bandwidth of 0.001, the noise component appears to be removed for edges with high frequency noise, while the other edge signals are not significantly altered.

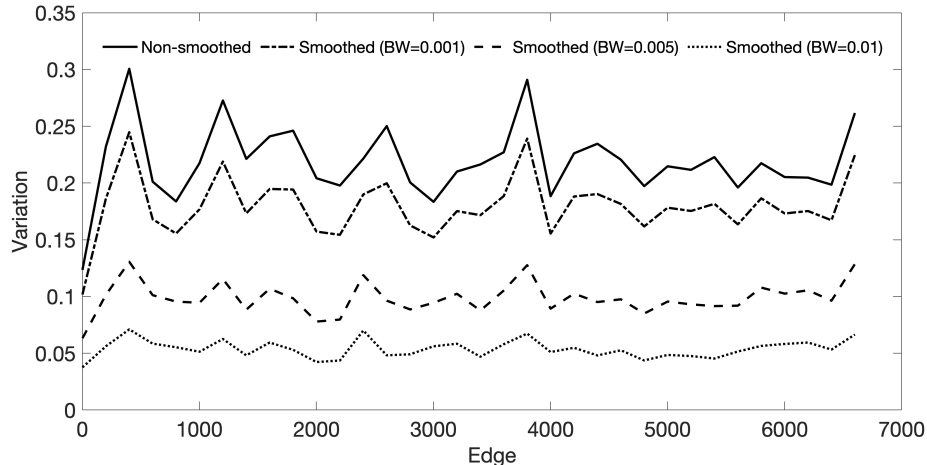


Fig. 6: Illustration of the level of variation with three diffusion bandwidths. A bandwidth (BW) of 0.001, 0.005, and 0.01 were applied to the connectivity maps. We observe that, irrespective of the given edge, the variation, quantified as the standard deviation at each edge across the 400 subjects is less for the smoothed connectivity matrices relative to the non-smoothed for either of the bandwidths.

Common 1-cycle basis across subjects If 1-cycle basis change from one subject to next, it is difficult to use the basis expansion itself as a feature statistical analysis. Thus, we propose to extract common 1-cycle basis in the network template obtained by averaging correlation matrices of all the subjects. Then we encode subject-level variability in the expansion coefficients with the fixed 1-cycle basis across subjects. To achieve this we used the average correlation matrix of all the networks as a functional network template. We then obtain $\mathcal{Q} = (p-1)(p-2)/2$ number of 1-cycle basis $\phi = [\mathcal{C}^1, \mathcal{C}^2, \dots, \mathcal{C}^{\mathcal{Q}}]$ for the functional template. Here ϕ denotes the common 1-cycle basis obtained from (9). Subsequently, the vectorized upper triangle entries of correlation matrix of each subject \mathcal{W} is expanded as

$$\mathcal{W} = \alpha_1 \mathcal{C}^1 + \alpha_2 \mathcal{C}^2 + \dots + \alpha_{\mathcal{Q}} \mathcal{C}^{\mathcal{Q}}.$$

The coefficients $\alpha = [\alpha_1, \dots, \alpha_{\mathcal{Q}}]^T$ are then estimated in the least squares fashion

$$\alpha = (\phi^T \phi)^{-1} \phi^T \mathcal{W}. \quad (15)$$

The estimated coefficients α for all the subjects are then used in discriminating two groups of networks Ω and Ψ . Let $\bar{\alpha}_j^{\Omega}$ and Let $\bar{\alpha}_j^{\Psi}$ be the mean of j -th 1-cycle basis in group Ω and Ψ respectively. Then we used the maxim difference

$$\mathcal{L}(\Omega, \Psi) = \max_{1 \leq j \leq \mathcal{Q}} |\bar{\alpha}_j^{\Omega} - \bar{\alpha}_j^{\Psi}| \quad (16)$$

as the test statistic in discriminating between two groups of networks. The statistical significance is determined using the permutation test. Unlike previous analysis that cannot localize specific cycles, the test statistic gives a way to localize most discriminating cycles by identifying the j -th cycle that gives the maximum.

2.6 Validation

Since cycles can be modelled to embed complex interactions, it can potentially uncover hidden topological patterns which are hitherto impossible in conventional graph models. We validate the proposed method in a simulation study with the ground truth. We generate

three types of networks with different number of loops. Some well known curved shapes such as a circle, lemniscate, quadrifolium [90] are chosen as the ground truth signal and then Gaussian noise is added $\mathcal{N}(0, 0.02^2)$ to the coordinates (Figure 4). The circle has a single loop, the lemniscate has two loops and the quadriform has four loops. The number of nodes to construct the network are chosen as $p = 64$ for all the types. This ensures we have the same number of cycles ($Q = 1953$ independent 1-cycles) in each type of simulated network.

Death values The topological distances between the simulated networks were measured by computing the 2-Wasserstein distance between 1D persistent diagram of 1-cycles. To compare between the different simulated loop structures, we generated five networks in each type (1-loop, 2-loops and 4-loops) such that they are clustered into three distinct groups. We then computed the pairwise Wasserstein distance between networks. Figure 4 shows the Wasserstein distance matrix between three groups. The clear clustering pattern demonstrates the Wasserstein distance applied to 1D topological feature works as expected. Networks with similar topology have smaller distances while networks with different topology have relatively large distances.

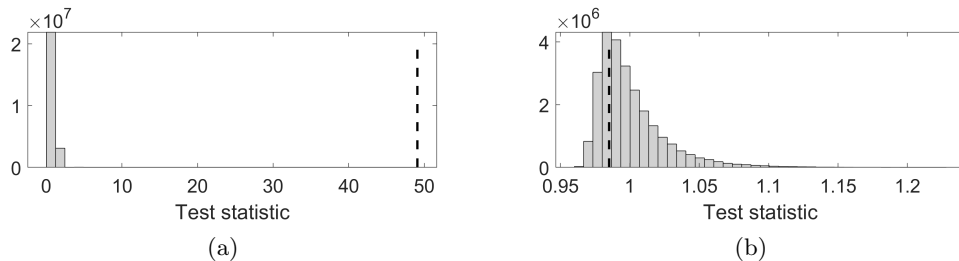


Fig. 7: An example of test statistics obtained for (a) network difference (1 vs 2) and (b) no network difference (2 vs 2). In the network difference, the observed statistic (dashed line) was 49.08 whereas in the no network difference case (1 vs 2) the observed statistic is 0.98.

Using the proposed ratio statistic, we computed p -values comparing different groups (Figure 7). Table 1 shows the average p -values obtained after 50 independent simulations. Each simulation is done with 100000 permutations. Networks of the same topology have large p -values indicating they are shown to be statistically not different. Networks of different topology have small p -values indicating they are shown to be statistically different. The results indicate the proposed method perform well in discriminating networks of different topology and not produces any false positives when there is no topological differences. Thus, the method perform well as expected. As the number of networks increase in each group, the p -values get smaller showing increased statistical power over increased sample size.

Length of cycles We used the maximum gap between sorted lengths of cycles as the test statistic. The tests are repeated for 10 times and the average p -values are reported. Each simulation is done with 100000 permutations. Table 2 shows the p -values obtained for this study. The p -values are low for networks with differences while the values are large when the network has no difference. However, in some situations, the test is not performing well. In the 2 vs 4 comparison, p -values are above not necessarily smaller than 0.05. This implies the length based test procedure is slightly weak. This can be easily remedied if we denoise high frequency noises in networks and redo the analysis.

Table 1: The performance results of Wasserstein distance on 1-cycles are summarized as average p -values for testing various combinations of cycles. Here 1 vs 2 means we compare the circle (1-loop) against a lemniscate (2-loops) and the columns 6 networks, 8 networks, 10 networks and 12 networks indicate the number of networks that we consider for each type. The smaller p -values indicate that our method can discriminate network differences.

loop-type	6 networks	8 networks	10 networks	12 networks
1 vs. 2	1.4×10^{-3}	6.8×10^{-5}	6.1×10^{-6}	4.4×10^{-7}
1 vs. 4	1.1×10^{-3}	5.4×10^{-5}	4.9×10^{-6}	5.2×10^{-7}
2 vs. 4	1.2×10^{-3}	6.6×10^{-5}	3.2×10^{-6}	2.0×10^{-7}
1 vs. 1	0.3954	0.5336	0.9790	0.7834
2 vs. 2	0.6516	0.8404	0.3458	0.5376
4 vs. 4	0.5943	0.8294	0.7561	0.5403

Clustering on Wasserstein distance We applied the method to the simulation study example in Figure 4. We have 3 groups of networks and 5 networks in each group, which is the ground truth. We averaged 50 different simulation results. We did k -means clustering using the MATLAB default function `kmeans.m`. We obtained the clustering accuracy of 1.0000 ± 0.0000 when input are sorted death values. In comparison, the clustering accuracy is 0.6187 ± 0.0774 when input are correlations.

Table 2: The performance results of length of cycles based test statistics on 1-cycles are summarized as average p -values for testing various combinations of cycles. Here 1 vs 2 means we compare the circle (1-loop) against a lemniscate (2-loops) and the columns 6 networks, 8 networks, 10 networks and 12 networks indicate the number of networks that we consider in each type. The smaller p -values indicate that our method can discriminate network differences.

loop-type	6 networks	8 networks	10 networks	12 networks
1 vs. 2	2.3×10^{-3}	1.6×10^{-4}	1.0×10^{-5}	0.0000
1 vs. 4	2.2×10^{-3}	2.1×10^{-5}	3.0×10^{-5}	0.0000
2 vs. 4	0.7921	0.4835	0.2277	0.6824
1 vs. 1	0.6197	0.6436	0.4631	0.5914
2 vs. 2	0.9377	0.8689	0.9040	0.2436
4 vs. 4	0.3069	0.9874	0.2730	0.6247

Common 1-cycles basis across subjects We used the maximum gap between coefficients of 1-cycle basis as the test statistic on the same simulation study. The tests are repeated for 10 times and the average p -values are reported. Each simulation is done with 100000 permutations. Table 3 shows the p -values obtained for this study. The p -values are low for networks with differences while the values are large when the network has no difference. The method performed better than the cycle length based analysis.

Table 3: The performance results of common 1-cycle basis are summarized as average p -values for testing various combinations of cycles. Here 1 vs 2 means we compare the circle (1-loop) against a lemniscate (2-loops) and the columns 6 networks, 8 networks, 10 networks and 12 networks indicate the number of networks that we consider for each type. The smaller p -values indicate that our method can discriminate network differences.

loop-type	6 networks	8 networks	10 networks	12 networks
1 vs. 2	2.1×10^{-3}	2.0×10^{-4}	1.0×10^{-5}	0.0000
1 vs. 4	1.9×10^{-3}	1.2×10^{-4}	2.0×10^{-5}	0.0000
2 vs. 4	1.8×10^{-3}	1.4×10^{-4}	1.0×10^{-5}	0.0000
1 vs. 1	0.4263	0.6606	0.8736	0.6735
2 vs. 2	0.3962	0.8919	0.9620	0.5590
4 vs. 4	0.7988	0.7365	0.4598	0.9815

3 Application

3.1 Dataset and preprocessing

In this study, we used the the subset of the resting-state fMRI data collected in the Human Connectome Project (HCP) [91,92]. The fMRI data were acquired for approximately 15 minutes for each scan. The participants are at rest with eyes open with relaxed fixation on a projected bright cross-hair on a dark back-ground[92]. The fMRI data were collected on a customized Siemens 3T Connectome Skyra scanner using a gradient-echoplanar imaging (EPI) sequence with multiband factor 8, repetition time (TR) 720ms, time echo (TE) 33.1ms, flip angle 52°, 104 × 90 (RO × PE) matrix size, 72 slices, 2mm isotropic voxels, and 1200 time points is used.

The standard minimal preprocessing pipelines [93] such as spatial distortion removal [94,95], motion correction [96,97], bias field reduction [98], registration to the structural MNI template, and data masking using the brain mask obtained from FreeSurfer [93] is performed on the fMRI scans. This resulted in the resting-state functional time series with $91 \times 109 \times 91$, 2mm isotropic voxels at 1200 time points. The subjects were in the age group ranging from 22 to 36 years with average age 29.24 ± 3.39 years for 172 males and 240 females. Subsequently, the Automated Anatomical Labeling (AAL) template was applied to parcellate the brain volume into 116 non-overlapping anatomical regions [99]. The fMRI across voxels within each brain parcellation is averaged (spatial denoising), resulting in 116 average fMRI time series with 1200 time points for each subject.

The scrubbing is done to remove fMRI volumes with spatial artifacts in functional connectivity [100,101,102,103] due to significant head motion [100,104]. The framewise displacement (FD) from the three translational displacements and three rotational displacements at each time point to measure the head movement from one volume to the next is calculated. The volumes with FD larger than 0.5mm and their neighbors were scrubbed [100,101,104]. About 12 subjects having excessive head movement are excluded from the dataset, resulting in a refined fMRI dataset of 400 subjects (168 males and 232 females). Additional details on the dataset can be found here [54,104].

3.2 Cycle computation

For each subject, we measured the whole-brain functional connectivity by computing the Pearson correlation matrix $\rho = (\rho_{ij})$ over while time points across 116 brain regions resulting in 400 correlation matrices of size 116×116 . Since the dataset contains $p = 116$ nodes, the total number of edges in the brain network is computed as $q = p(p - 1)/2 = 6670$. The edges in the transformed correlation matrix is now decomposed into birth and death sets following Theorem 1. The number of edges in the birth set is $\mathcal{P} = p - 1 = 116 - 1 = 115$.

The number of edges in the death set is $\mathcal{Q} = q - \mathcal{P} = 6555$. The edges from the death set are then sequentially added to the birth set to generate a sequence of 6555 subnetworks. Each subnetwork has only one cycle which is identified using the Hodge Laplacian.

Figure 8 shows how the number of the topological invariants β_0 (number of connected components) β_1 (number of cycles) changes over graph filtration on edge weights $w = (w_{ij})$. β_0 remains at one for a long duration and begins to increase towards the end and eventually reaches 116 which is the number of independent components or nodes. On the other hand, β_1 begins with $\mathcal{Q} = 6555$ cycles for a complete network and then gradually keeps decreasing as the edges are removed sequentially and goes to zero when all the cycles are dead. Once all the cycles are identified and extracted we primarily consider the death values of cycles. These topological quantities are used as test statistics for discriminating males from females.

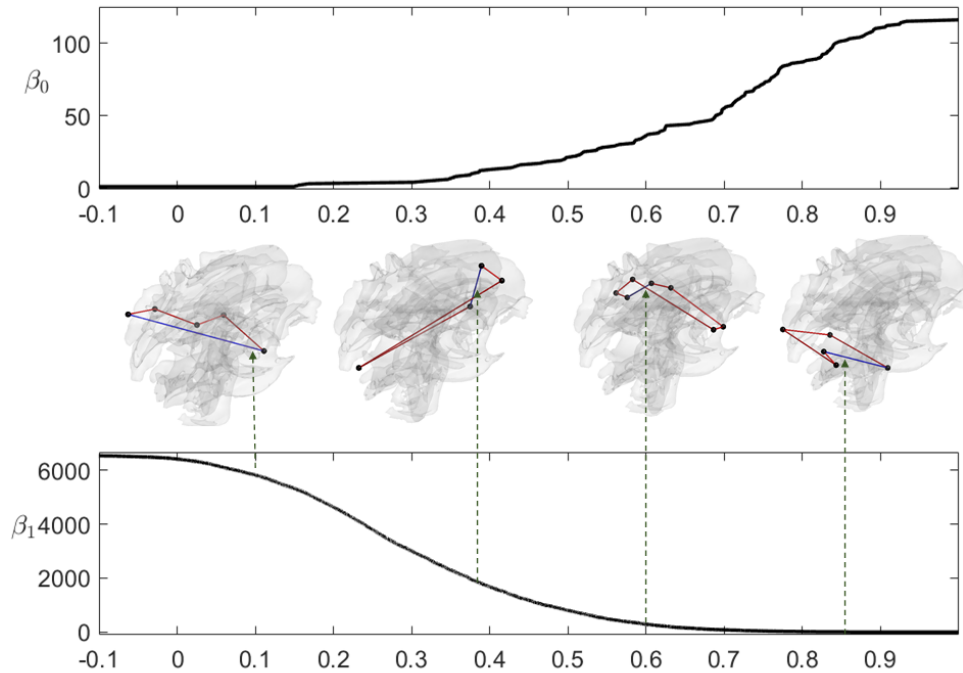


Fig. 8: Graph filtration of the average brain network of 400 subjects. β_0 is monotonically increasing while β_1 is monotonically decreasing. over the graph filtration. We have total 6555 cycles in the brain network. Middle: Four 1-cycles chosen at specific death values are shown. The edge weights are set to a constant value to visualize the cycles. The edges that destroy the cycles are shown in blue color.

3.3 The topological features of 1-cycles

The topological similarity between the networks can be measured by computing the 2-Wasserstein distance between persistent diagrams [54]. A distance matrix is constructed considering the pairwise Wasserstein distance between the subjects. Once we have the distance matrix, the group statistics can be carried out by calculating the within and between group statistics. Since the permutation test is computationally more demanding we adapt a scalable computation strategy using transpositions [82], which results in the p -value of 0.03. The transposition test is applied to determine the statistical significance in discrim-

inating the 232 females and 168 male subjects. The observed test statistic is 1.0232 and corresponding p -value is 0.04 based for 500000 random transpositions (Figure 9-(a)).

We also accessed the topological disparity between the groups using the length of the cycle. The test statistics were formulated for the length of the cycles following the proposed procedure. The observed statistic was found to be $\mathcal{L} = 0.303$ which corresponds to p -value of 0.64 based on 500000 random permutations (Figure 9-(b)). Based on the simulation study and real data, we conclude that the death values of cycles seem to be useful feature but the length of cycles are not useful discriminating features of cycles.

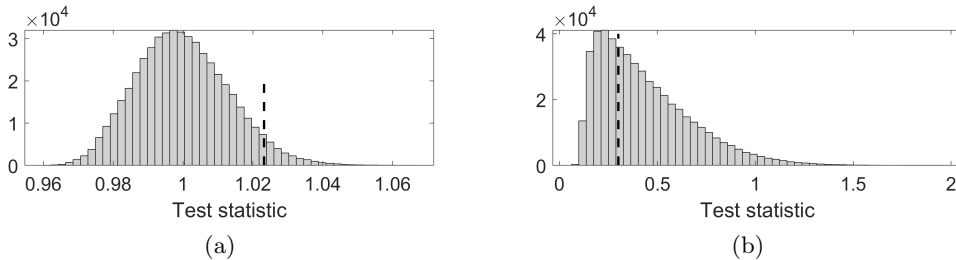


Fig. 9: (a) The histogram of the ratio statistic on death values with p -value of 0.04. (b) The histogram of the maximum gap statistic on cycle length with p -value of 0.64.

We also performed Wasserstein clustering by feeding sorted death values of the brain networks to the built-in MATLAB k -means clustering function `kmeans.m`. Since the k -means algorithm is sensitive to initial cluster centers, we used different initializations of centers. We then averaged the result of 50 independent run of k -means algorithm. We obtained the clustering accuracy of 0.6361 ± 0.1065 demonstrating cycles as a potential discriminating features in brain network clustering. In comparison, k -means clustering applied to correlations directly produced the clustering accuracy of 0.5790 ± 0.0816 [105].

3.4 Common 1-cycle basis

The common 1-cycle basis on the average correlation matrices of 400 subjects is extracted after heat diffusion on correlation matrices. We solved for the coefficients for each network using equation (15). We computed the mean coefficients for females and males separately for each cycle. We then used the maximum difference between mean coefficients as the test statistic. The observed statistic was found to be 0.434, which corresponds to p -value of 0.007. The statistical inference is based on 500000 permutations. The first, second and third maximum difference was found to be 0.434, 0.400 and 0.362 which correspond to the cycle basis 5021th, 2939th and 673th respectively. Figure 10 shows three most discriminating cycles. The top row is males and bottom row is females. The edges represent the average correlation in each group. It is seen that the coefficient vector when used as topological feature can differentiate the male and female network.

4 Conclusions

A cycle in the brain network is one of the most fundamental topological features that one has to identify, extract and quantify in order to understand and model higher order interactions. In this work, an efficient scalable algorithm to identify and extract the 1-cycles in a network is proposed. We combine the ideas from persistent homology and the Hodge Laplacian to facilitate an easy detection of 1-cycles. The method is demonstrated with an illustration and applied to the resting state brain networks from Human Connectome Project (HCP).

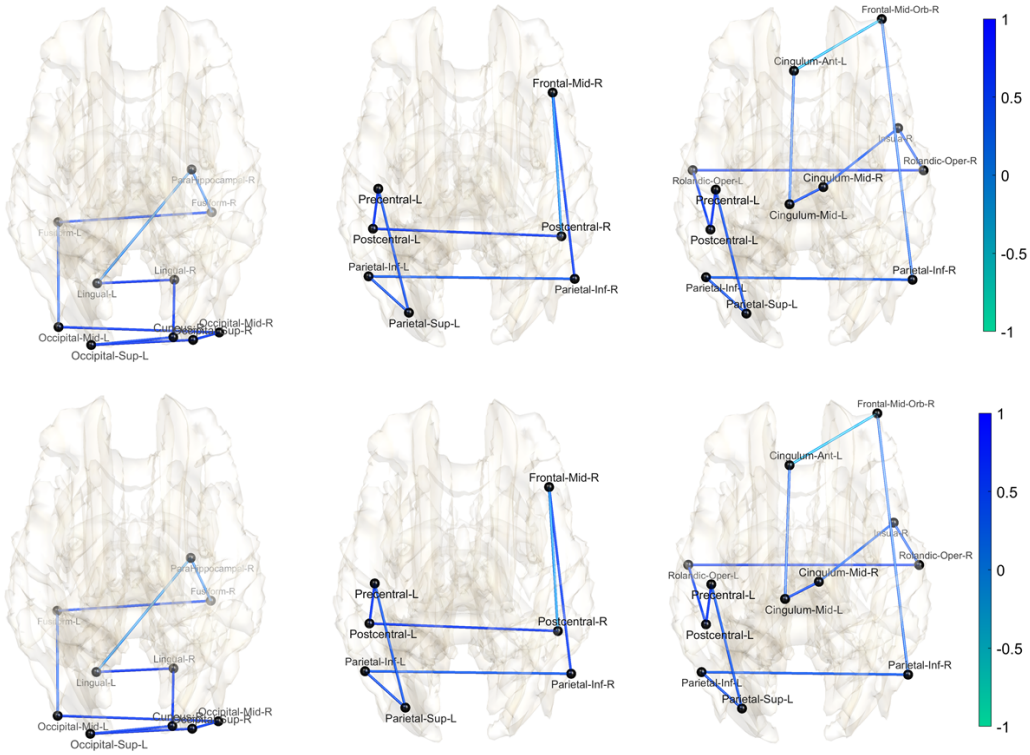


Fig. 10: The three most discriminating cycles corresponding to maximum values in the test statistics namely., 5021th, 2939th and 673th cycle basis are shown. Top: male and Bottom: female dataset.

The proposed algorithm is efficient for typical brain network data which has few hundred nodes ($p \sim 100$). Even for larger networks ($p \sim 1000$), computation can be done quickly in $\mathcal{O}(p \log p)$ run time through the maximum spanning trees (MST).

One of our major goals in the study is to discriminate networks having different loops. To capture this topological characteristic, we used the 1-cycle basis to precisely encode this information without redundancy. Although the information about the number of loops is present in the cycle basis, sometimes it can get hidden or lost in the large number of cycles. It is not even clear how to represent all the cycles without overlaps. Through the combination of MST and the Hodge Laplacian, we were able to extract and represent 1-cycle basis as a sparse matrix.

We designed a new topological inference procedure based on the 1-cycle attributes such as length and death values of cycles. These statistical frameworks are used to examine in discriminating the brain networks of males and females. Our studies emphasize that it is meaningful to study and model the higher order interactions using the 1-cycle basis for brain network analysis.

Based on the proposed 1-cycle basis, any cycle in the graph can be represented as linear combination of basis: $\sum_{j=1}^Q \alpha_j \mathcal{C}^j$. Such vectorization enables us to build more complex models such as sparse network models [49] or joint identification of common cycles across subjects [106]. This is left as a future study. The Wasserstein distance between cycles \mathcal{C}^i and \mathcal{C}^j is simply the squared difference of death values $(d_i - d_j)^2$. Such squared norm makes computation involving cycles straightforward.

Acknowledgements

We thank Kelin Xia of Nanyang Technological University for discussion and support of the project. We also like to thank Shih-Gu Huang of National University of Singapore for providing support for fMRI processing. We also thank Soumya Das of University of Wisconsin-Madison for discussion on length based analysis. This study is funded by NIH R01 EB022856, EB02875, NSF MDS-2010778. All the sections were written by Anand except the sections on network clustering written by Wang and the sections on heat diffusion written by Dakurah.

References

1. P. J. Uhlhaas and W. Singer, “Neural synchrony in brain disorders: relevance for cognitive dysfunctions and pathophysiology,” *Neuron*, vol. 52, no. 1, pp. 155–168, 2006.
2. P. J. Uhlhaas and W. Singer, “Abnormal neural oscillations and synchrony in schizophrenia,” *Nature Reviews Neuroscience*, vol. 11, no. 2, pp. 100–113, 2010.
3. H. J. Park and K. Friston, “Structural and functional brain networks: from connections to cognition,” *Science*, vol. 342, no. 6158, 2013.
4. R. F. Betzel and D. S. Bassett, “Multi-scale brain networks,” *Neuroimage*, vol. 160, pp. 73–83, 2017.
5. P. J. Uhlhaas, G. Pipa, B. Lima, L. Melloni, S. Neuenschwander, D. Nikolić, and W. Singer, “Neural synchrony in cortical networks: history, concept and current status,” *Frontiers in Integrative Neuroscience*, vol. 3, p. 17, 2009.
6. L. Pessoa, “Understanding brain networks and brain organization,” *Physics of Life Reviews*, vol. 11, no. 3, pp. 400–435, 2014.
7. R. Ghorbanchian, J. G. Restrepo, J. J. Torres, and G. Bianconi, “Higher-order simplicial synchronization of coupled topological signals,” *Communications Physics*, vol. 4, no. 1, pp. 1–13, 2021.
8. O. Sporns, “Graph theory methods: applications in brain networks,” *Dialogues in Clinical Neuroscience*, vol. 20, no. 2, p. 111, 2018.
9. C. J. Stam and J. C. Reijneveld, “Graph theoretical analysis of complex networks in the brain,” *Nonlinear Biomedical Physics*, vol. 1, no. 1, pp. 1–19, 2007.
10. E. T. Bullmore and O. Sporns, “Complex brain networks: graph theoretical analysis of structural and functional systems,” *Nature Reviews Neuroscience*, vol. 10, no. 3, pp. 186–198, 2009.
11. S. de Lange, M. de Reus, and M. Van Den Heuvel, “The Laplacian spectrum of neural networks,” *Frontiers in Computational Neuroscience*, vol. 7, p. 189, 2014.
12. C. Hu, L. Cheng, J. Sepulcre, K. A. Johnson, G. E. Fakhri, Y. M. Lu, and Q. Li, “A spectral graph regression model for learning brain connectivity of Alzheimer’s disease,” *PloS One*, vol. 10, no. 5, p. e0128136, 2015.
13. E. T. Bullmore and D. S. Bassett, “Brain graphs: graphical models of the human brain connectome,” *Annual Review of Clinical Psychology*, vol. 7, pp. 113–140, 2011.
14. X. N. Zuo, R. Ehmke, M. Mennes, D. Imperati, F. X. Castellanos, O. Sporns, and M. P. Milham, “Network centrality in the human functional connectome,” *Cerebral Cortex*, vol. 22, no. 8, pp. 1862–1875, 2012.
15. M. E. Newman, “Finding community structure in networks using the eigenvectors of matrices,” *Physical Review E*, vol. 74, no. 3, p. 036104, 2006.
16. O. Sporns, C. J. Honey, and R. Kötter, “Identification and classification of hubs in brain networks,” *PloS One*, vol. 2, no. 10, p. e1049, 2007.
17. M. P. van den Heuvel and O. Sporns, “Network hubs in the human brain,” *Trends in Cognitive Sciences*, vol. 17, no. 12, pp. 683–696, 2013.
18. C. Giusti, R. Ghrist, and D. S. Bassett, “Two’s company, three (or more) is a simplex,” *Journal of Computational Neuroscience*, vol. 41, no. 1, pp. 1–14, 2016.
19. F. Battiston, G. Cencetti, I. Iacopini, V. Latora, M. Lucas, A. Patania, J.-G. Young, and G. Petri, “Networks beyond pairwise interactions: structure and dynamics,” *Physics Reports*, vol. 874, pp. 1–92, 2020.
20. P. Skardal and A. Arenas, “Higher order interactions in complex networks of phase oscillators promote abrupt synchronization switching,” *Communications Physics*, vol. 3, pp. 1–6, 2020.

21. L. Torres, A. S. Blevins, D. Bassett, and T. Eliassi-Rad, “The why, how, and when of representations for complex systems,” *SIAM Review*, vol. 63, no. 3, pp. 435–485, 2021.
22. E. N. Davison, K. J. Schlesinger, D. S. Bassett, M.-E. Lynall, M. B. Miller, S. T. Grafton, and J. M. Carlson, “Brain network adaptability across task states,” *PLoS Computational Biology*, vol. 11, no. 1, p. e1004029, 2015.
23. E. N. Davison, B. O. Turner, K. J. Schlesinger, M. B. Miller, S. T. Grafton, D. S. Bassett, and J. M. Carlson, “Individual differences in dynamic functional brain connectivity across the human lifespan,” *PLoS Computational Biology*, vol. 12, no. 11, p. e1005178, 2016.
24. B. Jie, C. Y. Wee, D. Shen, and D. Zhang, “Hyper-connectivity of functional networks for brain disease diagnosis,” *Medical Image Analysis*, vol. 32, pp. 84–100, 2016.
25. C. Zu, Y. Gao, B. Munsell, M. Kim, Z. Peng, J. R. Cohen, D. Zhang, and G. Wu, “Identifying disease-related subnetwork connectome biomarkers by sparse hypergraph learning,” *Brain Imaging and Behavior*, vol. 13, no. 4, pp. 879–892, 2019.
26. G. Carlsson, “Topology and data,” *Bulletin of the American Mathematical Society*, vol. 46, no. 2, pp. 255–308, 2009.
27. H. Edelsbrunner, J. Harer, *et al.*, “Persistent homology—a survey,” *Contemporary Mathematics*, vol. 453, pp. 257–282, 2008.
28. M. K. Chung, H. Lee, A. DiChristofano, H. Ombao, and V. Solo, “Exact topological inference of the resting-state brain networks in twins,” *Network Neuroscience*, vol. 3, no. 3, pp. 674–694, 2019.
29. M. K. Chung, V. Vilalta Gil, P. J. Rathouz, B. B. Lahey, and D. H. Zald, “Mapping heritability of large-scale brain networks with a billion connections via persistent homology,” *arXiv preprint arXiv:1509.04771*, 2015.
30. A. E. Sizemore, J. E. Phillips Cremins, R. Ghrist, and D. S. Bassett, “The importance of the whole: topological data analysis for the network neuroscientist,” *Network Neuroscience*, vol. 3, no. 3, pp. 656–673, 2019.
31. M. K. Chung, H. Lee, V. Solo, R. J. Davidson, and S. D. Pollak, “Topological distances between brain networks,” in *International Workshop on Connectomics in Neuroimaging*, pp. 161–170, Springer, 2017.
32. Y. Wang, H. Ombao, and M. K. Chung, “Topological data analysis of single-trial electroencephalographic signals,” *The Annals of Applied Statistics*, vol. 12, no. 3, p. 1506, 2018.
33. G. Petri, M. Scolamiero, I. Donato, and F. Vaccarino, “Topological strata of weighted complex networks,” *PloS One*, vol. 8, no. 6, p. e66506, 2013.
34. H. Lee, M. K. Chung, H. Kang, B.-N. Kim, and D. S. Lee, “Computing the shape of brain networks using graph filtration and Gromov-Hausdorff metric,” in *International Conference on Medical Image Computing and Computer-Assisted Intervention*, pp. 302–309, Springer, 2011.
35. H. Lee, H. Kang, M. K. Chung, B.-N. Kim, and D. S. Lee, “Persistent brain network homology from the perspective of dendrogram,” *IEEE transactions on medical imaging*, vol. 31, no. 12, pp. 2267–2277, 2012.
36. H. Lee, M. K. Chung, H. Kang, and D. S. Lee, “Hole detection in metabolic connectivity of alzheimer’s disease using k-laplacian,” in *International Conference on Medical Image Computing and Computer-Assisted Intervention*, pp. 297–304, Springer, 2014.
37. M. W. Reimann, M. Nolte, M. Scolamiero, K. Turner, R. Perin, G. Chindemi, P. Dłotko, R. Levi, K. Hess, and H. Markram, “Cliques of neurons bound into cavities provide a missing link between structure and function,” *Frontiers in Computational Neuroscience*, vol. 11, p. 48, 2017.
38. G. Petri, P. Expert, F. Turkheimer, R. Carhart Harris, D. Nutt, P. J. Hellyer, and F. Vaccarino, “Homological scaffolds of brain functional networks,” *Journal of The Royal Society Interface*, vol. 11, no. 101, p. 20140873, 2014.
39. B. Tadić, M. Andjelković, and R. Melnik, “Functional geometry of human connectomes,” *Scientific Reports*, vol. 9, no. 1, pp. 1–12, 2019.
40. P. G. Lind, M. C. Gonzalez, and H. J. Herrmann, “Cycles and clustering in bipartite networks,” *Physical Review E*, vol. 72, no. 5, p. 056127, 2005.
41. R. Tarjan, “Depth-first search and linear graph algorithms,” *SIAM Journal on Computing*, vol. 1, no. 2, pp. 146–160, 1972.
42. H. Lee, M. K. Chung, H. Kang, H. Choi, Y. K. Kim, and D. S. Lee, “Abnormal hole detection in brain connectivity by kernel density of persistence diagram and Hodge Laplacian,” in *2018 IEEE 15th International Symposium on Biomedical Imaging (ISBI 2018)*, pp. 20–23, IEEE, 2018.

43. O. Sporns, G. Tononi, and G. M. Edelman, "Theoretical neuroanatomy: relating anatomical and functional connectivity in graphs and cortical connection matrices," *Cerebral Cortex*, vol. 10, no. 2, pp. 127–141, 2000.
44. M. K. Chung, S. G. Huang, A. Gritsenko, L. Shen, and H. Lee, "Statistical inference on the number of cycles in brain networks," in *2019 IEEE 16th International Symposium on Biomedical Imaging (ISBI 2019)*, pp. 113–116, IEEE, 2019.
45. H. Edelsbrunner and J. Harer, *Computational Topology: an introduction*. American Mathematical Society., 2010.
46. C. Chen and D. Freedman, "Measuring and computing natural generators for homology groups," *Computational Geometry*, vol. 43, no. 2, pp. 169–181, 2010.
47. A. Muhammad and M. Egerstedt, "Control using higher order laplacians in network topologies," in *Proc. of 17th International Symposium on Mathematical Theory of Networks and Systems*, pp. 1024–1038, Citeseer, 2006.
48. F. R. Chung and F. C. Graham, *Spectral graph theory*. No. 92, American Mathematical Society., 1997.
49. M. K. Chung, J. L. Hanson, J. Ye, R. J. Davidson, and S. D. Pollak, "Persistent homology in sparse regression and its application to brain morphometry," *IEEE Transactions on Medical Imaging*, vol. 34, no. 9, pp. 1928–1939, 2015.
50. H. Edelsbrunner, D. Letscher, and A. Zomorodian, "Topological persistence and simplification," in *Proceedings 41st Annual Symposium on Foundations of Computer Science*, pp. 454–463, IEEE, 2000.
51. K. Xia and G. W. Wei, "Persistent homology analysis of protein structure, flexibility, and folding," *International Journal for Numerical Methods in Biomedical Engineering*, vol. 30, no. 8, pp. 814–844, 2014.
52. J. R. Munkres, *Elements of algebraic topology*. CRC press, 2018.
53. M. K. Chung, V. Villalta Gil, H. Lee, P. J. Rathouz, B. B. Lahey, and D. H. Zald, "Exact topological inference for paired brain networks via persistent homology," in *International Conference on Information Processing in Medical Imaging*, pp. 299–310, Springer, 2017.
54. T. Songdechakraiwut and M. K. Chung, "Topological learning for brain networks," *arXiv preprint arXiv:2012.00675*, 2020.
55. R. Ghrist, "Barcodes: the persistent topology of data," *Bulletin of the American Mathematical Society*, vol. 45, no. 1, pp. 61–75, 2008.
56. R. J. Adler, O. Bobrowski, M. S. Borman, E. Subag, and S. Weinberger, "Persistent homology for random fields and complexes," in *Borrowing strength: theory powering applications—a Festschrift for Laurence D. Brown*, pp. 124–143, Institute of Mathematical Statistics, 2010.
57. K. Mischaikow and V. Nanda, "Morse theory for filtrations and efficient computation of persistent homology," *Discrete & Computational Geometry*, vol. 50, no. 2, pp. 330–353, 2013.
58. Y. Mileyko, S. Mukherjee, and J. Harer, "Probability measures on the space of persistence diagrams," *Inverse Problems*, vol. 27, no. 12, p. 124007, 2011.
59. J. J. Berwald, J. M. Gottlieb, and E. Munch, "Computing Wasserstein distance for persistence diagrams on a quantum computer," *arXiv preprint arXiv:1809.06433*, 2018.
60. J. R. Munkres, "Algorithms for the assignment and transportation problems," *Journal of the Society for Industrial and Applied Mathematics*, vol. 5, no. 1, pp. 32–38, 1957.
61. Z. Su, Y. Wang, R. Shi, W. Zeng, J. Sun, F. Luo, and X. Gu, "Optimal mass transport for shape matching and comparison," *IEEE Transactions on Pattern Analysis and Machine Intelligence*, vol. 37, no. 11, pp. 2246–2259, 2015.
62. Z. Su, W. Zeng, Y. Wang, Z. L. Lu, and X. Gu, "Shape classification using Wasserstein distance for brain morphometry analysis," in *International Conference on Information Processing in Medical Imaging*, pp. 411–423, Springer, 2015.
63. J. Edmonds and R. M. Karp, "Theoretical improvements in algorithmic efficiency for network flow problems," *Journal of the Association for Computing Machinery*, vol. 19, no. 2, pp. 248–264, 1972.
64. J. Rabin, G. Peyré, J. Delon, and M. Bernot, "Wasserstein barycenter and its application to texture mixing," in *International Conference on Scale Space and Variational Methods in Computer Vision*, pp. 435–446, Springer, 2011.
65. S. S. Vallender, "Calculation of the Wasserstein distance between probability distributions on the line," *Theory of Probability & Its Applications*, vol. 18, no. 4, pp. 784–786, 1974.
66. G. D. Canas and L. Rosasco, "Learning probability measures with respect to optimal transport metrics," *arXiv preprint arXiv:1209.1077*, 2012.

67. J. Chen, R. Zhao, Y. Tong, and G. W. Wei, “Evolutionary de Rham-Hodge method,” *arXiv preprint arXiv:1912.12388*, 2019.
68. Z. Meng and K. Xia, “Persistent spectral-based machine learning (PerSpect ML) for protein-ligand binding affinity prediction,” *Science Advances*, vol. 7, no. 19, p. eabc5329, 2021.
69. D. Horak and J. Jost, “Spectra of combinatorial Laplace operators on simplicial complexes,” *Advances in Mathematics*, vol. 244, pp. 303–336, 2013.
70. S. Barbarossa and S. Sardellitti, “Topological signal processing over simplicial complexes,” *IEEE Transactions on Signal Processing*, vol. 68, pp. 2992–3007, 2020.
71. M. T. Schaub, A. R. Benson, P. Horn, G. Lippner, and A. Jadbabaie, “Random walks on simplicial complexes and the normalized hodge 1-laplacian,” *SIAM Review*, vol. 62, no. 2, pp. 353–391, 2020.
72. S. Mukherjee and J. Steenbergen, “Random walks on simplicial complexes and harmonics,” *Random structures & Algorithms*, vol. 49, no. 2, pp. 379–405, 2016.
73. A. Zomorodian, “Fast construction of the Vietoris-Rips complex,” *Computers & Graphics*, vol. 34, no. 3, pp. 263–271, 2010.
74. L. H. Lim, “Hodge Laplacians on graphs,” *SIAM Review*, vol. 62, no. 3, pp. 685–715, 2020.
75. J. Friedman, “Computing Betti numbers via combinatorial Laplacians,” *Algorithmica*, vol. 21, no. 4, pp. 331–346, 1998.
76. M. K. Chung, Z. Luo, A. D. Leow, A. L. Alexander, R. J. Davidson, and H. H. Goldsmith, “Exact combinatorial inference for brain images,” in *International Conference on Medical Image Computing and Computer-Assisted Intervention*, pp. 629–637, Springer, 2018.
77. P. M. Thompson, T. D. Cannon, K. L. Narr, T. Van Erp, V. P. Poutanen, M. Huttunen, J. Lönqvist, C. G. Standertskjöld Nordenstam, J. Kaprio, M. Khaledy, *et al.*, “Genetic influences on brain structure,” *Nature Neuroscience*, vol. 4, no. 12, pp. 1253–1258, 2001.
78. A. Zalesky, A. Fornito, I. H. Harding, L. Cocchi, M. Yücel, C. Pantelis, and E. T. Bullmore, “Whole-brain anatomical networks: does the choice of nodes matter?,” *Neuroimage*, vol. 50, no. 3, pp. 970–983, 2010.
79. T. E. Nichols and A. P. Holmes, “Nonparametric permutation tests for functional neuroimaging: a primer with examples,” *Human Brain Mapping*, vol. 15, no. 1, pp. 1–25, 2002.
80. A. M. Winkler, G. R. Ridgway, G. Douaud, T. E. Nichols, and S. M. Smith, “Faster permutation inference in brain imaging,” *Neuroimage*, vol. 141, pp. 502–516, 2016.
81. W. Feller, *An introduction to probability theory and its applications, vol 2*. John Wiley & Sons, 2008.
82. M. K. Chung, L. Xie, S. G. Huang, Y. Wang, J. Yan, and L. Shen, “Rapid acceleration of the permutation test via transpositions,” in *International Workshop on Connectomics in Neuroimaging*, pp. 42–53, Springer, 2019.
83. A. P. Kulkarni, M. K. Chung, B. B. Bendlin, and V. Prabhakaran, “Investigating heritability across resting state brain networks via heat kernel smoothing on persistence diagrams,” in *2020 IEEE 17th International Symposium on Biomedical Imaging Workshops (ISBI Workshops)*, pp. 1–4, IEEE, 2020.
84. H. Le and A. Kume, “The fréchet mean shape and the shape of the means,” *Advances in Applied Probability*, pp. 101–113, 2000.
85. K. Turner, Y. Mileyko, S. Mukherjee, and J. Harer, “Fréchet means for distributions of persistence diagrams,” *Discrete & Computational Geometry*, vol. 52, pp. 44–70, 2014.
86. Y. Zemel and V. Panaretos, “Fréchet means and procrustes analysis in Wasserstein space,” *Bernoulli*, vol. 25, pp. 932–976, 2019.
87. P. Dubey and H.-G. Müller, “Fréchet analysis of variance for random objects,” *Biometrika*, vol. 106, pp. 803–821, 2019.
88. M. K. Chung, A. Qiu, S. Seo, and H. K. Vorperian, “Unified heat kernel regression for diffusion, kernel smoothing and wavelets on manifolds and its application to mandible growth modeling in ct images,” *Medical image analysis*, vol. 22, no. 1, pp. 63–76, 2015.
89. M. K. Chung, Y. Wang, and G. Wu, “Heat kernel smoothing in irregular image domains,” *arXiv preprint arXiv:1710.07849*, 2017.
90. R. C. Yates, “Curves and their properties.” 1974.
91. D. C. Van Essen, K. Ugurbil, E. Auerbach, D. Barch, T. E. Behrens, R. Bucholz, A. Chang, L. Chen, M. Corbetta, S. W. Curtiss, *et al.*, “The Human Connectome Project: a data acquisition perspective,” *Neuroimage*, vol. 62, no. 4, pp. 2222–2231, 2012.
92. D. C. Van Essen, S. M. Smith, D. M. Barch, T. E. Behrens, E. Yacoub, K. Ugurbil, W.-M. H. Consortium, *et al.*, “The WU-Minn human connectome project: an overview,” *Neuroimage*, vol. 80, pp. 62–79, 2013.

93. M. F. Glasser, S. N. Sotiropoulos, J. A. Wilson, T. S. Coalson, B. Fischl, J. L. Andersson, J. Xu, S. Jbabdi, M. Webster, J. R. Polimeni, *et al.*, “The minimal preprocessing pipelines for the Human Connectome Project,” *Neuroimage*, vol. 80, pp. 105–124, 2013.
94. J. L. Andersson, S. Skare, and J. Ashburner, “How to correct susceptibility distortions in spin-echo echo-planar images: application to diffusion tensor imaging,” *Neuroimage*, vol. 20, no. 2, pp. 870–888, 2003.
95. J. Jovicich, S. Czanner, D. Greve, E. Haley, A. van Der Kouwe, R. Gollub, D. Kennedy, F. Schmitt, G. Brown, J. MacFall, *et al.*, “Reliability in multi-site structural mri studies: effects of gradient non-linearity correction on phantom and human data,” *Neuroimage*, vol. 30, no. 2, pp. 436–443, 2006.
96. M. Jenkinson and S. Smith, “A global optimisation method for robust affine registration of brain images,” *Medical Image Analysis*, vol. 5, no. 2, pp. 143–156, 2001.
97. M. Jenkinson, P. Bannister, M. Brady, and S. Smith, “Improved optimization for the robust and accurate linear registration and motion correction of brain images,” *Neuroimage*, vol. 17, no. 2, pp. 825–841, 2002.
98. M. F. Glasser and D. C. Van Essen, “Mapping human cortical areas in vivo based on myelin content as revealed by T1-and T2-weighted MRI,” *Journal of Neuroscience*, vol. 31, no. 32, pp. 11597–11616, 2011.
99. N. Tzourio Mazoyer, B. Landeau, D. Papathanassiou, F. Crivello, O. Etard, N. Delcroix, B. Mazoyer, and M. Joliot, “Automated anatomical labeling of activations in SPM using a macroscopic anatomical parcellation of the MNI MRI single-subject brain,” *Neuroimage*, vol. 15, no. 1, pp. 273–289, 2002.
100. J. D. Power, K. A. Barnes, A. Z. Snyder, B. L. Schlaggar, and S. E. Petersen, “Spurious but systematic correlations in functional connectivity MRI networks arise from subject motion,” *Neuroimage*, vol. 59, no. 3, pp. 2142–2154, 2012.
101. K. R. Van Dijk, M. R. Sabuncu, and R. L. Buckner, “The influence of head motion on intrinsic functional connectivity MRI,” *Neuroimage*, vol. 59, no. 1, pp. 431–438, 2012.
102. T. D. Satterthwaite, D. H. Wolf, J. Loughhead, K. Ruparel, M. A. Elliott, H. Hakonarson, R. C. Gur, and R. E. Gur, “Impact of in-scanner head motion on multiple measures of functional connectivity: relevance for studies of neurodevelopment in youth,” *Neuroimage*, vol. 60, no. 1, pp. 623–632, 2012.
103. C. Caballero Gaudes and R. C. Reynolds, “Methods for cleaning the BOLD fMRI signal,” *Neuroimage*, vol. 154, pp. 128–149, 2017.
104. S. G. Huang, S. B. Samdin, C.-M. Ting, H. Ombao, and M. K. Chung, “Statistical model for dynamically-changing correlation matrices with application to brain connectivity,” *Journal of Neuroscience Methods*, vol. 331, p. 108480, 2020.
105. S.-G. Huang, S.-T. Samdin, C. Ting, H. Ombao, and M. Chung, “Statistical model for dynamically-changing correlation matrices with application to brain connectivity,” *Journal of Neuroscience Methods*, vol. 331, p. 108480, 2020.
106. H. Lee, M. K. Chung, H. Kang, H. Choi, S. Ha, Y. Huh, E. Kim, and D. S. Lee, “Coidentification of group-level hole structures in brain networks via Hodge Laplacian,” in *International Conference on Medical Image Computing and Computer-Assisted Intervention*, pp. 674–682, Springer, 2019.